We are IntechOpen,
the world's leading publisher of
Open Access books
Built by scientists, for scientists

6,900
Open access books available

185,000
International authors and editors

200M
Downloads

154
Countries delivered to

Our authors are among the

TOP 1%
most cited scientists

12.2%
Contributors from top 500 universities

CLARIVATE ANALYTICS
BOOK CITATION INDEX
INDEXED

WEB OF SCIENCE™

Selection of our books indexed in the Book Citation Index
in Web of Science™ Core Collection (BKCI)

Interested in publishing with us?
Contact book.department@intechopen.com

Formation of Various Nanocarbon and Composite Structures by Laser Ablation

Fumio Kokai
Mie University
Japan

1. Introduction

Nanocarbon and composite materials have attracted considerable research attention due to their unique properties and potential applications. Laser ablation of graphite or graphite containing a small amount of metals can produce various nanocarbon structures such as single-walled (SW) (Guo et al., 1995) and multi-walled carbon nanotubes (MWCNTs) (Hirahara et al., 2000), SW carbon nanohorn (CNH) aggregates (Iijima et al., 1999) and polyhedral graphite (PG) particles (Kokai et al., 2003). In this chapter, we describe a simple method to form various nanocarbon and composite structures using laser ablation in high-pressure Ar gas up to 0.9 MPa, with particular focus on the composite nanostructures. Graphite targets containing metals or compounds (Si, Fe, Co, Ni, Cu, Ag, B_4C, Y_2O_3, La_2O_3, and Gd_2O_3) were used as source materials. To effectively form nanocarbon and composite structures by laser irradiation onto the targets at room temperature, we used a continuous wave Nd:YAG laser to eject C and other species with relatively low kinetic energies into the high-pressure Ar gas. As a result, hot C and metal species are confined in a space surrounded by Ar gas. For example, the initial temperature of the vaporized C species was ~5000 °C estimated for laser irradiation from emission spectroscopy (Kokai et al., 2001). In addition, emission imaging and shadowgraphic studies implied that vaporized species had low expansion velocities of 10^2–10^3 cm/s (Kokai et al., 1999) due to the high-pressure Ar gas restricting their expansion. Unlike a laser ablation method combined with an electric furnace for SW and MWCNT growth, where vaporized C and metal species kept at 800–1300°C are essential for an efficient CNT growth (Gorbunov et al., 1999), the heat sources available for the growth of various nanocarbon and composite structures in this study are laser-ablated C and metal species themselves confined by high-pressure Ar gas. The control of the resident densities and the maintenance of high-temperature of laser-ablated C and metal species, based on adjusting the metal content in graphite and the Ar gas pressure, results in various composite nanostructures with high yields in the deposits. The nanostructures were characterized using scanning electron microscopy (SEM), transmission electron microscopy (TEM), selected area electron diffraction (SAED) and x-ray diffraction (XRD) patterns, and Raman spectroscopy. Depending on the type and content of metals and compounds, characteristic nanocarbon and composite structures such as hybridized SWCNH particles and Cu- or SiC-filled one-dimensional (1D) structures were formed. We discuss the metal-dependent growth of the various nanocarbon and composite structures with an emphasis on graphitization processes such as thermal graphitization, catalytic graphitization and vapor-

liquid-solid (VLS) growth (Wagner & Ellis, 1964), and unconventional VLS growth without a catalyst.

2. Experimental

A set of elements, Si, Fe, Co, Ni, Cu, and Ag, and compounds, B_4C, Y_2O_3, La_2O_3, and Gd_2O_3, were mixed with graphite and with metal contents typically from 5 to 30 atomic (at.) %. For B_4C and Si, higher contents were used up to 60 (B content) and 70 at.%, respectively. The average particle sizes of the graphite, Si, Fe, Co, Ni, Cu, Ag, B_4C, Y_2O_3, La_2O_3, and Gd_2O_3 powders were 5, 45, 20, 2, 3, 2, 100, 60, 30, 40, and 30 μm, respectively. The mixed powders were ground and then pressed to form pellets (10 mm in diameter, 2 mm thick) under a pressure of 10 MPa in a stainless-steel die press. A continuous wave Nd:YAG laser (500 W peak power) was used for the laser ablation at room temperature. The laser beam was focused on the pellets through a quartz window installed on a cylindrical stainless-steel chamber (110 mm in diameter and 150 mm long) filled with Ar gas at pressures ranging from 0.05 to 0.9 MPa, as in previous studies (Kokai et al., 2003 and 2004). The size of the laser spot and the power density were adjusted to 2 mm and approximately 13–23 kW/cm², respectively, and the laser irradiation time was set to 2 s. After laser irradiation of several shots on the fresh surface of a rotating target, the depsits produced on the chamber wall were collected. The deposits were examined with a SEM and TEMs operated at 100 kV and 300 kV. XRD measurements of the deposits were carried out using Cu-Kα radiation operated at 40 kV and 150 mA. Raman spectra of the deposits were taken with excitation by means of the 488-nm line of an Ar⁺ laser.

3. Characterization of nanocarbon and composite structures

3.1 Hybridized SWCNH and other particles from graphite containing Fe, Co, Ni, or Ag

SWCNH particles with diameters of 80–100 nm are almost spherical aggregates of many tubule-like structures made of graphitic sheets (Iijima et al., 1999). Room-temperature CO_2 laser ablation of graphite can produce SWCNH particles with a high yield of over 90%. Comparing the growth of SWCNH particles with those of other nanostructured graphitic carbons, platelet graphite (PLG) (Kokai et al., 2004) and PG particles (Kokai et al., 2003), grown under different Ar gas pressure conditions up to 0.8 MPa has suggested that the formation of tubule-like SWCNH structures and their aggregation in Ar gas was important for the formation of SWCNH particles (Kokai et al., 2004). The generation of a new hybrid structure, a SWCNH particle including a Ni-encapsulated carbon nanocapsule (CNC) in its center, was reported using a submerged arc method (Sano et al., 2004). The CNC is a hollow graphitic cage filled with iron-group or rare-earth metals and it has a typical diameter of 10–200 nm (Ruoff et al., 1993; Saito, 1995). However, the major product that was formed was Ni-encapsulated CNCs using the submerged arc method. The SWCNH particles hybridized with the CNCs had a very low (less than 1%) yield.

The laser ablation of graphite containing Fe, Co, Ni, or Ag produced SWCNH particles hybridized with CNCs with a high yield of ~70% and other nanostructures at Ar gas pressures of 0.1–0.3 MPa (Kobayashi et al., 2007). Figures 1a–d show typical TEM images of four products obtained by the laser ablation of a graphite-Fe target. The Fe content was 20 at.% in the target. The products shown here, which include Fe core particles, are a SWCNH particle, a PLG particle (Kokai et al., 2004), an amorphous carbon (AC) particle, and a CNC.

The Fe cores in the SWCNH, PLG, and AC particles were smaller than those of the CNCs. In addition to the core particles, small Fe particles often attached with the AC particles (Fig. 1c). This may be due to a higher concentration of defects in the AC particles.
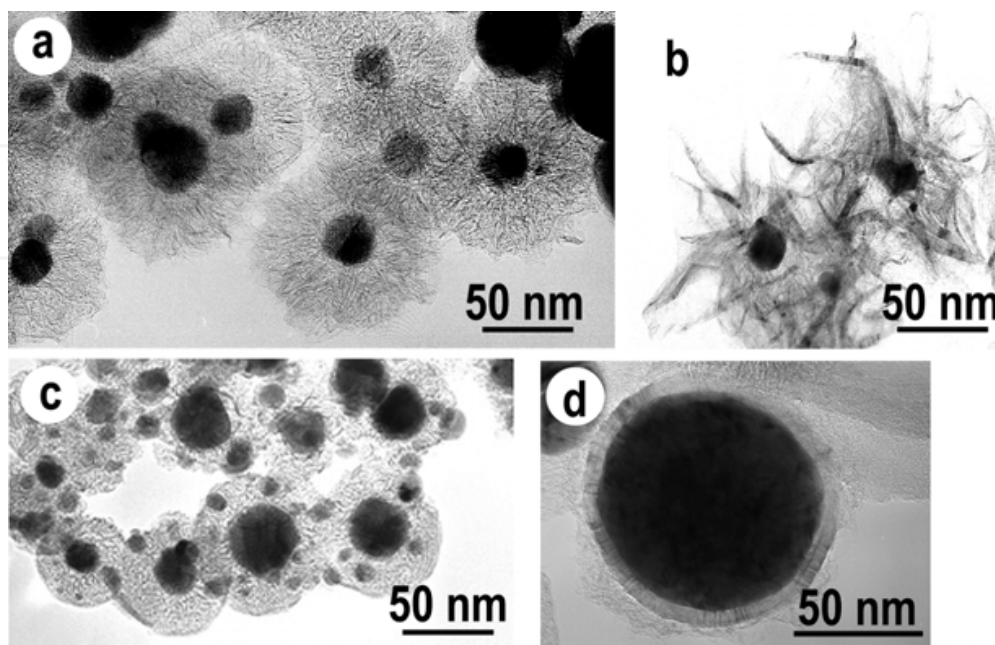

Fig. 1. TEM images of hybridized (a) SWCNH, (b) PLG, and (c) AC particles and (d) CNC obtained by laser ablation of graphite containing 20 at.% Fe and at Ar gas pressures of 0.1–0.3 MPa.

The outer region of one of the hybridized SWCNH particles is magnified in Fig. 2a, showing horn structures, similar to those of unhybridized SWCNH aggregates. The core region is also magnified in Fig. 2b. Graphitic layers cover the core just like in CNCs. These layers ranged in number from 10 to 25. The presence of these layers is similar to the SWCNH particles hybridized with Ni-containing CNCs. Similar graphitic layers were frequently observed as the cores of the PLG and AC particles. To identify the phase of the Fe core in the hybridized SWCNH particle, a SAED pattern and its corresponding lattice image were taken (Fig. 2c). The SAED pattern consists of two types of patterns: annular rings from graphitic layers and spots from the core. Several sets of spots were superimposed because the core was polycrystalline. Spots diffracted from a grain can easily be distinguished by comparing them in the lattice image. The direction of the spot must be normal to the lattice fringes. The spots, indicated by the arrows in the image, can be assigned to the (1-22) and (211) reflections of an orthorhombic Fe_3C crystal according to the data of Joint Committee on Powder Diffraction Standards (JCPDS) No. 6-0670 (*Pbnm, a=0.452, b=0.507, and c=0.674 nm*). The measured d-values calculated from the nominal camera length were 0.198 and 0.188 nm, and the interplanar angle was 76°. These values can not be explained by assuming α-Fe or γ-Fe phases.

The yields of the four products shown in Figs. 1a–d were strongly dependent on the Ar gas pressure and the Fe content in the graphite target. We roughly estimated the yields of the four products by comparing their areas in TEM images measured for several parts in the deposits after laser irradiation. Figure 3 shows the yields of the four products as a function of the Ar gas pressure. Graphite targets containing 20 at.% Fe were used for each laser
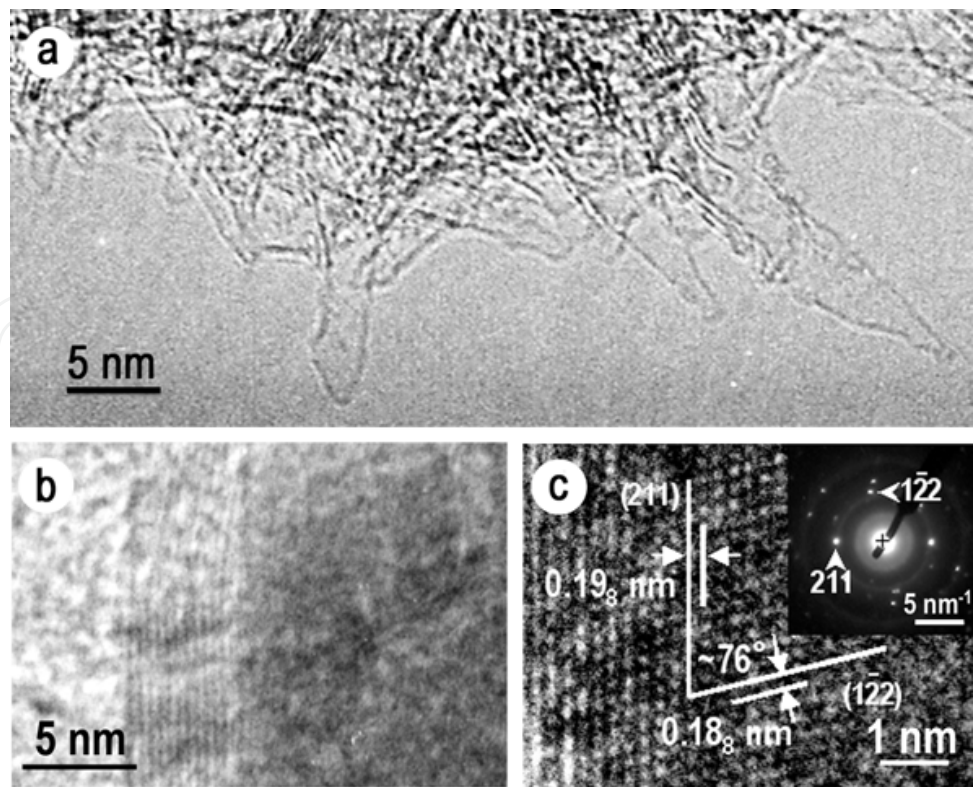
Fig. 2. TEM images observed in (a) the outer region and (b) near the core of a hybridized SWCNH particle and (c) the corresponding SAED pattern and lattice image.
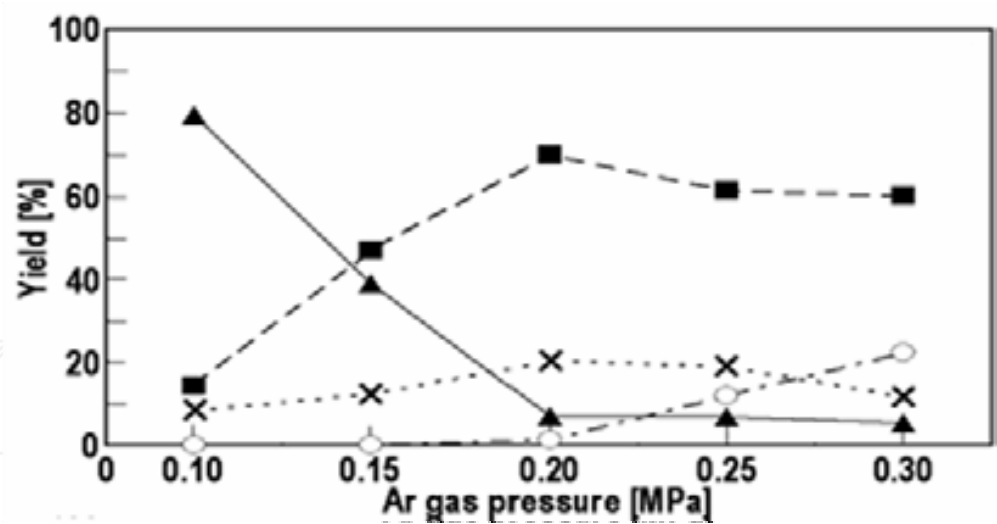

Fig. 3. Yields of hybridized SWCNH (■), AC (▲), and PLG (○) particles and CNCs (×) as a function of Ar gas pressure.

irradiation. At 0.1 MPa, the major product (~80%) was AC particles hybridized with Fe_3C particles or Fe_3C-filled CNCs. As the Ar gas pressure was increased, the yield of the hybridized AC particles decreased, while the yield of the SWCNH particles hybridized with Fe_3C-filled CNCs significantly increased. At 0.2 MPa, the yield of the hybridized SWCNH particles reached a maximum value of about 70%. Under this condition, almost all of the SWCNH particles contained Fe_3C-filled CNCs and the yield of unhybridized SWCNH

particles, which did not contain CNCs, was less than 1%. When the Ar gas pressure was further increased, the yield of the hybridized SWCNH particles decreased and the yield of hybridized PG particles only slightly increased.

In an XRD pattern (Fig. 4) of the product obtained from a 20 at.% Fe target at 0.2 MPa, where the hybridized SWCNH particles attained the highest yield, all the peaks, except for the one at 50.5°, were assigned to the reflections of a Fe_3C crystal. This was consistent with the SAED analysis shown in Fig. 2c. The XRD pattern also indicated that the Fe in the other products (~30%) was also in the carbide phase. We note that when we used Fe-free graphite for laser ablation, the yield of the SWCNH particles was highest at the same Ar gas pressure of 0.2 MPa and the yield of the PLG particles increased with a further increase in the Ar gas pressure. The formation of the SWCNH particles hybridized with Fe_3C-filled CNCs thus seems to depend on the aggregation of SWCNHs.

Figure 5 shows the dependence of the Fe content in a laser-irradiation graphite target on the yields of products. The Ar gas pressure was kept at 0.2 MPa for each laser ablation. As the Fe content increased from 5 at.%, the yield of the hybridized SWCNH particles increased and reached a maximum (~70%) at 20 at.%. For 5 and 10 at.% Fe, unhybridized SWCNH particles were observed and caused a reduction in the yield of hybridized SWCNH particles. After the maximum yield was reached, the hybridized SWCNH particle yield decreased, while the CNC yield increased drastically. In addition to the Fe_3C-filled CNCs, the number of Fe-filled CNCs, confirmed by an SAED pattern having spots of metallic α-Fe, increased. This Fe content dependence indicates that the existence of a suitable amount of Fe relative to the C in an Ar atmosphere is important for forming high-yield SWCNH particles hybridized with Fe_3C-filled CNCs. The CNC formation in environments of excess Fe hinders the formation of SWCNH particles like the Fe content of 30 at.% of Fig. 5.
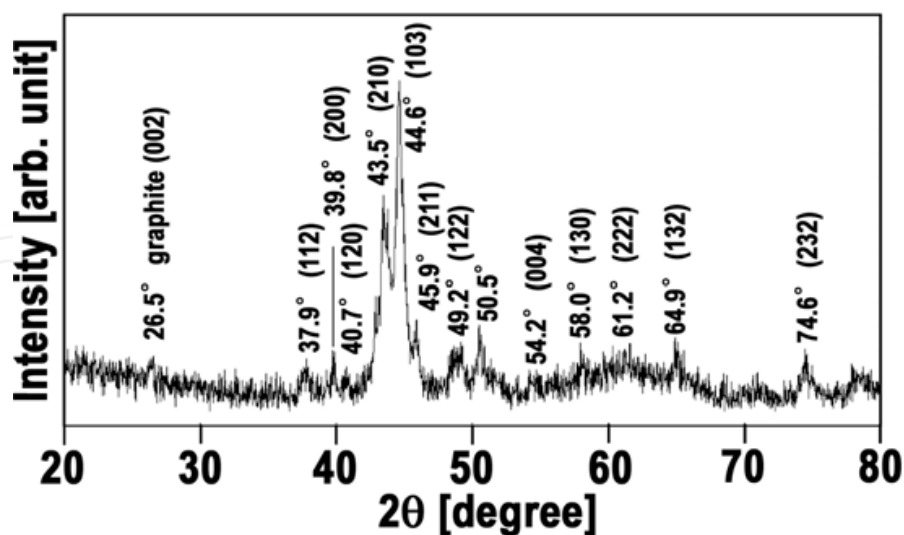

Fig. 4. XRD pattern of the product by laser ablation of graphite containing 20 at.% Fe at Ar gas pressure of 0.2 MPa. Most of the peaks are assigned to Fe_3C. The (110) and (200) reflections of α-Fe may overlap with the (103) and (132) reflections of Fe_3C, respectively, but the intensities of the (110) and (200) reflections are low, indicating a minor α-Fe product.
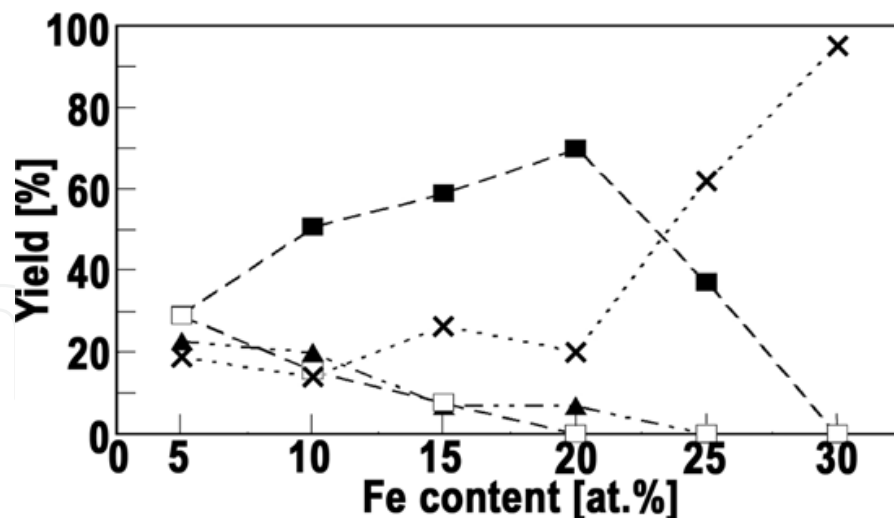
Fig. 5. Yields of unhybridized SWCNH particles (□), hybridized SWCNH particles (■), hybridized AC particles (▲), and CNCs (×) as a function of Fe content in the graphite target. The yield of the hybridized PLG particles (not shown) was at most 1%.

The formation of a metal- or carbide-filled CNCs is believed to occur through the precipitation of carbon from a supersaturated molten metal-C particle at a high temperature (Ruoff et al., 1993; Saito, 1995). On the basis of binary phase diagrams of metal and C (Massalski et al., 1990), the C solubility in a metal particle at a high temperature probably differs significantly depending on the type of metal used. Therefore, we attempted to fabricate hybrid structures of SWCNH particles and CNCs using graphite targets containing various metals. As a result, Co, Ni, and Ag were encapsulated to form hybridized SWCNH particles similar to that of Fe. Their yields were the highest (~70%) under the processing conditions, which were also similar to that used for Fe. For example, a TEM image of a hybridized SWCNH particle and the corresponding SAED pattern of a specimen formed using a graphite target containing 20 at.% Co and an Ar gas pressure of 0.2 MPa are shown in Fig. 6. According to JCPDS No. 15-0806, the spot indicated by the arrow in the SAED is assigned to β-Co (*fcc, α=0.354 nm*). Fast quenching may stabilize the meta-stable β-phase as was observed in the CNCs (Saito, 1995; Jiao et al., 1996). An XRD measurement (Fig. 7) also supported the quenching. All the peaks were successfully assigned to β-Co, except for the peak at 26.6° that reflected from graphite (002). It is important to note that the core was not a carbide but a metal, although the Co-C system contains carbides, such as Co_2C and Co_3C just like in the Fe-C system. The Ni and Ag cores were also metals rather than metal carbides. These metallic cores were also covered with graphitic layers, but they were thinner (1–15 layers) than those of the Fe_3C particles (10–25 layers).

In order to further analyze the detailed structures of the hybridized SWCNH particles, comparative TEM examination was performed for three types of hybridized SWCNH particles synthesized from graphite containing 20 at.% Fe, Co, or Ag (hereafter Fe, Co, and Ag hybrids) (Kokai et al., 2009). As shown in binary phase diagams (Massalski et al., 1990), Fe, Co, and Ag have significantly different C solubilities: 25, 4.2, and 0.036 at.%, respectively. From more than 200 samples for each hybridized structure (some samples can be seen in Fig. 8), the diameters of the hybrids and the encapsulated CNCs and the thicknesses of the SWCNH layers surrounding the CNCs were measured and compared.
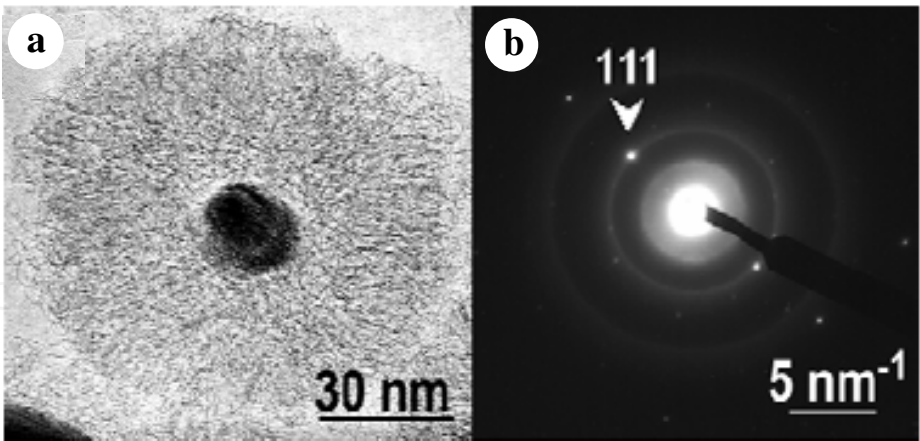
Fig. 6. (a) TEM image and (b) the corresponding SAED pattern of a product from graphite containing Co. The Co content in graphite was 20 at.%. The laser ablation experiments were carried out at Ar gas pressure of 0.2 MPa.
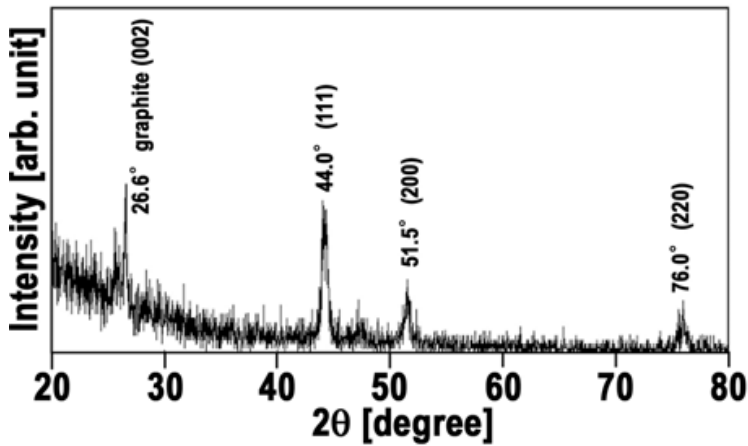

Fig. 7. XRD pattern of the product by laser ablation of graphite containing 20 at.% Co at Ar gas pressure of 0.2 MPa. The peaks are assigned to β-Co.
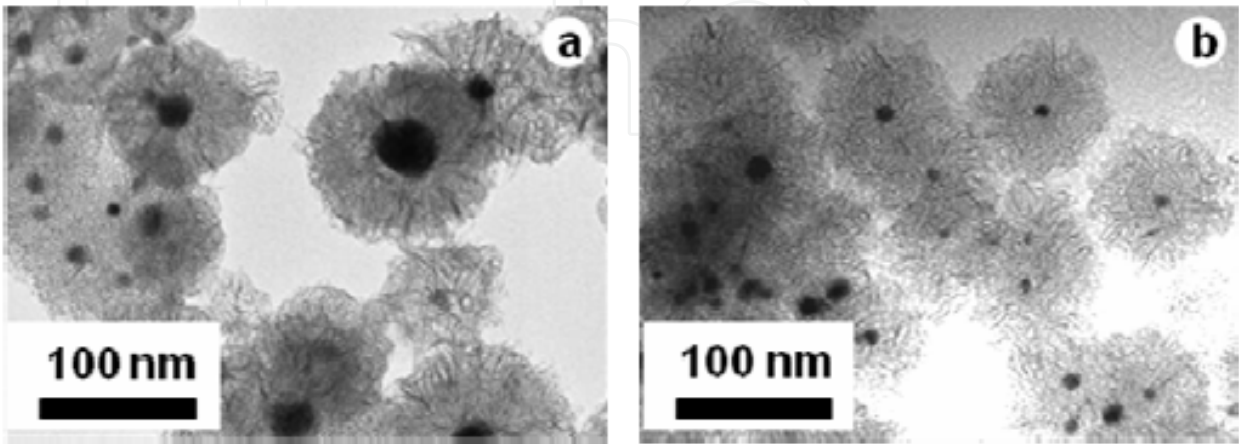

Fig. 8. TEM images of (a) Co and (b) Ag hybrids obtained by laser ablation of graphite containing 20 at.% Co or Ag at Ar gas pressure of 0.2 MPa.

Figure 9 shows diameter distributions of the hybrids (d_h) and CNCs (d_c) for the three hybrids. As shown in Fig. 9a, the d_h values for the three structures range from 40 to 150 nm; however the peak position and d_h distribution differ among the structures. The average d_h values are 96, 90, and 85 nm for the Fe, Co, and Ag hybrids, respectively. As shown in Fig. 9b, the d_c values range from 5 to 55 nm. The d_c distributions differ among the structures; the average diameters are 24, 19, and 16 nm for the Fe, Co, and Ag hybrids, respectively. Note that large CNCs with diameters up to ~140 nm, which were not surrounded by SWCNHs, were also observed, as in the previous study (Kobayashi et al., 2007). In addition to d_h and d_c, the distributions of the SWCNH layer thicknesses (t_n) were also measured for the three hybrids (not shown). The t_n values ranged from 15 to 65 nm. The average t_n values were
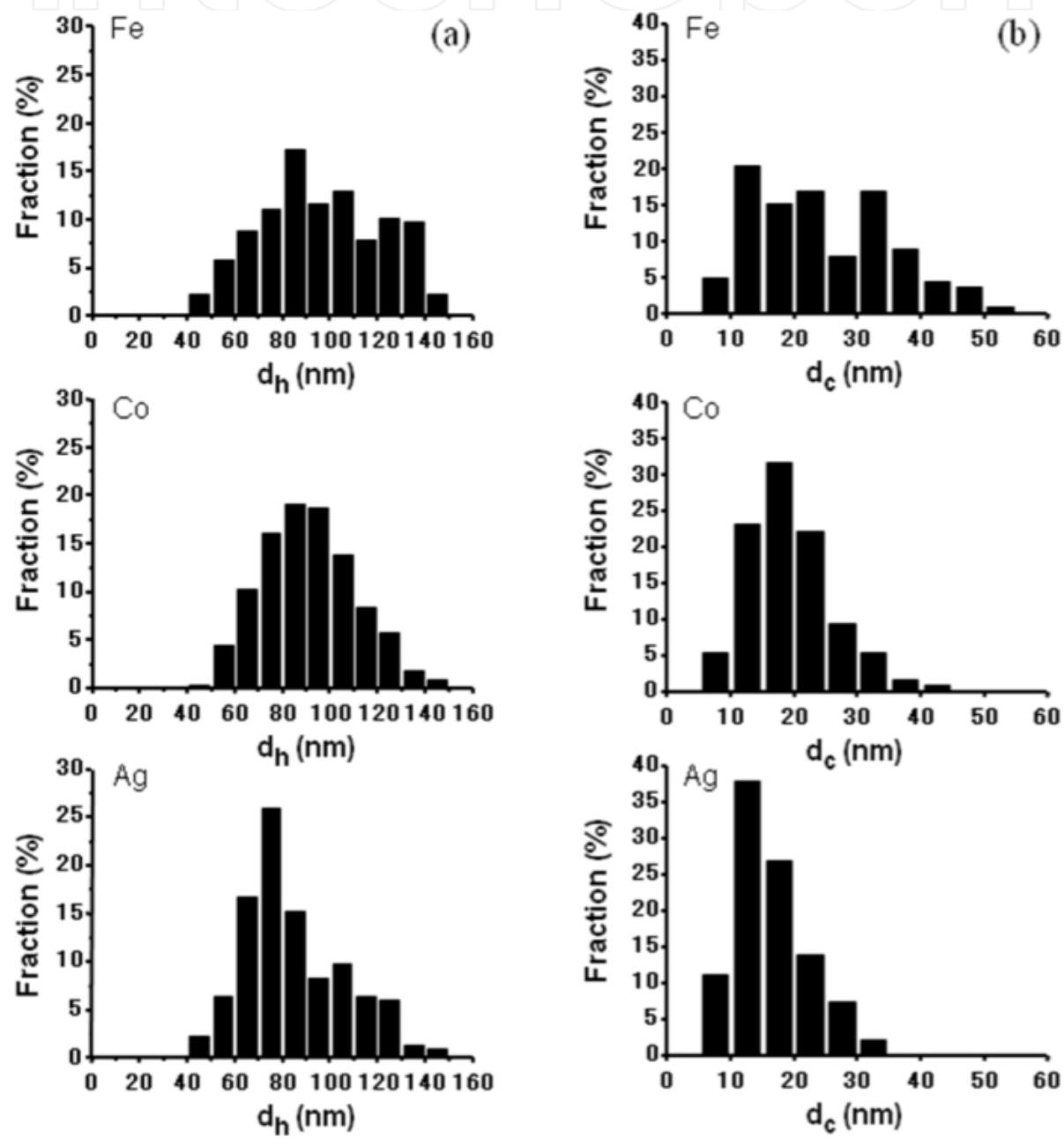

Fig. 9. Diameter distributions of the (a) hybrids (d_h) and (b) CNCs (d_c) for Fe, Co, and Ag hybrids.

18 nm for the Fe and Co hybrids and 17 nm for the Ag hybrid. Unlike the d_h and d_c values, no significant difference was observed in the average t_n values among the three hybrids.

The distributions of d_h, d_c, and t_n and their average values indicate that the difference in the diameters of the three hybrids is due to the formation of CNCs with different diameters in accordance with the type of metal. From the solublites of C for Fe, Co, and Ag, we believe that the diameters of the CNCs in the hybrids are governed by the differences in the C solubilities and precipitation processes. The stronger ability of Fe to form a carbide probably results in CNCs with larger sizes.

For the three hybrids, we investigated the correlation of d_h with d_c or $2t_n$. Figures 10 and 11 show plots of d_h versus d_c or $2t_n$ for the three hybrids. Although d_h increases with both d_c and $2t_n$, there is a stronger correlation between d_h and $2t_n$. For the Fe, Co, and Ag hybrids, the correlation coefficients were calculated to be 0.82, 0.74, and 0.70 between d_h and d_c and 0.94, 0.96, and 0.97 between d_h and $2t_n$. The correlation of d_h with $2t_n$ may be stronger because the lengths of the SWCNHs account for a considerable portion of the hybrid diameter.

In addition to the different d_h distributions for the three hybrids and stronger correlation between d_h and $2t_n$, some interesting features were observed regarding the formation mechanism of the hybridized SWCNH particles. Change in the metal contents in the graphite target resulted in the formation of unhybridized products (Fig. 5). In particular, when the content of the metal in graphite was lower than 20 at.%, we observed both hybrids and unhybridized SWCNH particles.
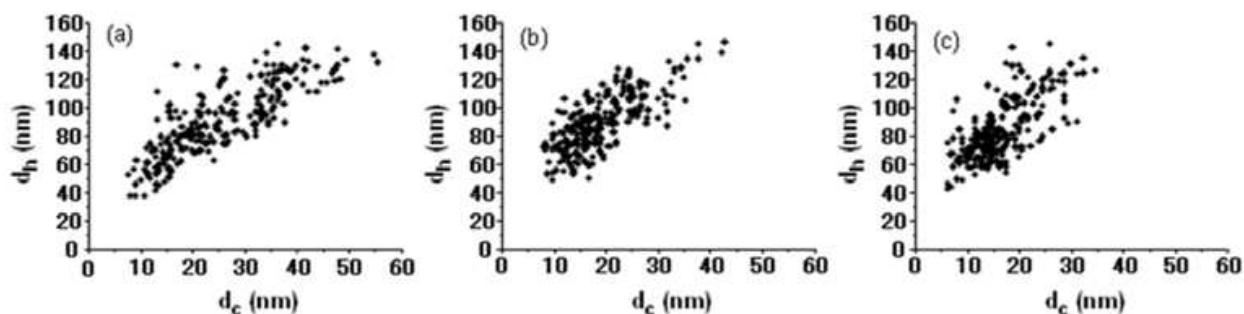

Fig. 10. Plots of hybrid diameter (d_h) versus CNC diameter (d_c) for (a) Fe, (b) Co, and (c) Ag hybrids.
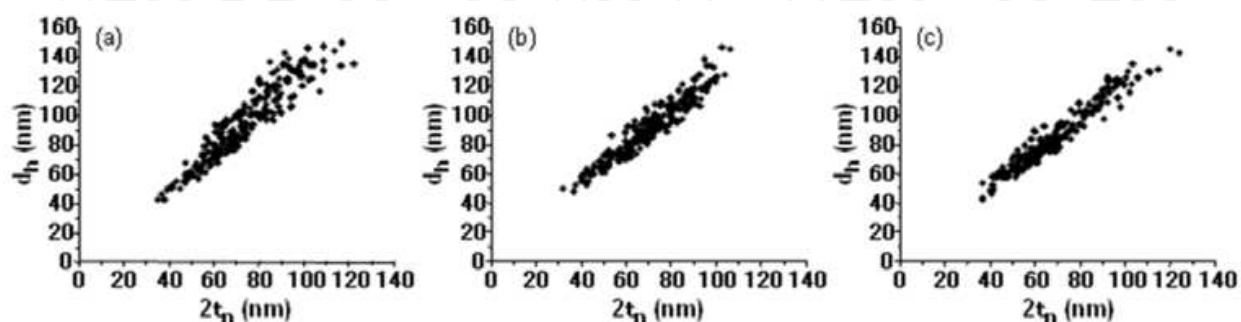

Fig. 11. Plots of hybrid diameter (d_h) versus twice the SWCNH layer thickness ($2t_n$) for (a) Fe, (b) Co, and (c) Ag hybrids.

Figure 12a shows a typical TEM image of the products produced at an Ar pressure of 0.2 MPa and with an Fe content of 10 at.%. There are Fe hybrids and unhybridized SWCNH

aggregates; the diameters of the unhybridized SWCNH aggregates are less than those of the Fe hybrids. As the metal content in the graphite target was increased from 20 at.%, the numbers of hybrids and SWCNH aggregates decreased and the number of unhybridized CNCs rapidly increased (Fig. 5). Figure 12b shows a typical TEM image of the products produced at an Ar gas pressure of 0.2 MPa and with an Fe content of 30 at.%. There are many CNCs with diameters of 20–210 nm. The preferable formation of molten metal-C particles probably consumes the carbon source and hinders the formation of SWCNHs into hybrid structures (Fig. 5).
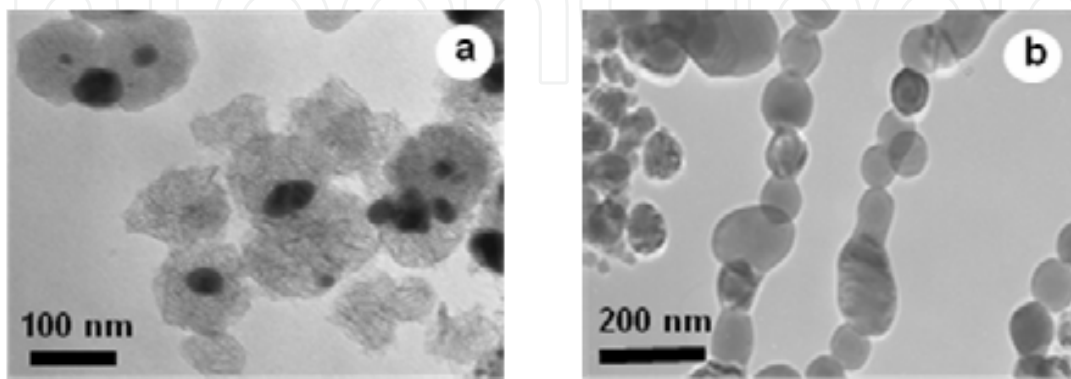

Fig. 12. TEM images of products obtained by laser ablation of graphite containing (a) 10 and (b) 30 at.% Fe at Ar gas pressure of 0. 2 MPa.

From some of the present findings, we propose a mechanism for hybrid formation, which is based on SWCNHs assembling around a molten metal-C particle as a nucleation core. After laser ablation of graphite containing metal, vaporized hot C and metal species form molten metal-C particles together with many SWCNHs and/or their precursors like graphene patches (Kawai et al., 2002) in a space confined by Ar gas. By using a differential mobility analyzer, the evolution in the size distribution of C particles was analyzed after laser ablation and C particles, 20–120 nm in size, were detected (Cheng at al., 2007), while the formation of SWCNHs and/or their precursors probably due to thermal graphitization is not clear The strong correlation between the hybrid diameter and the SWCNH layer thickness for Fe, Co, and Ag hybrids (Fig. 11) suggests that after the SWCNHs with a certain range of lengths are formed, they aggregate around molten metal-C particles with a certain range of diameters.
The contribution of only small CNCs (Figs. 9b and 10) to the hybrid formation suggests that the mutual interaction among SWCNHs near the center of the hybrid structure plays a crucial role in maintaining the resultant aggregate structure, while CNCs with diameters of 20–210 nm were formed. The increase in the numbers of covering graphitic layers due to the annealing of the CNCs at 600–1100°C (Jiao & Seraphin, 1998) and the graphitization of carbon (diamond and AC) by metal (catalytic graphitization) at 600–1000°C (Yudasaka et al., 2002) indicates that C precipitation, which leads to the formation of CNCs in SWCNH aggregates, occurs after SWCNH assembly. The growth of the hybridized SWCNH particle involves two graphitization processes, one thermal and the other catalytic.

3.2 Sea-urchin type SWCNTs and carbide-filled PG particles from graphite containing Y_2O_3, La_2O_3, and Gd_2O_3

The laser ablation of graphite containing Y_2O_3, La_2O_3, and Gd_2O_3 did not produce hybridized SWCNH particles and provided products composed of sea-urchin type SWCNTs

and C polyhedra filled with carbide particles dependent on the Ar gas pressure (Kokai et al., 2008). For example, Fig. 13 shows a TEM image of the product made from graphite containing 20 at.% Y_2O_3 at an Ar gas pressure of 0.1 MPa. Sea-urchin type SWCNTs, which are radially arranged around a catalytic particle as formed in a previous study using an arc discharge method (Subramoney et al., 1993), are grown from a yttrium carbide particle with a diameter of ~20 nm. The SWCNTs were short, with lengths up to only ~50 nm.
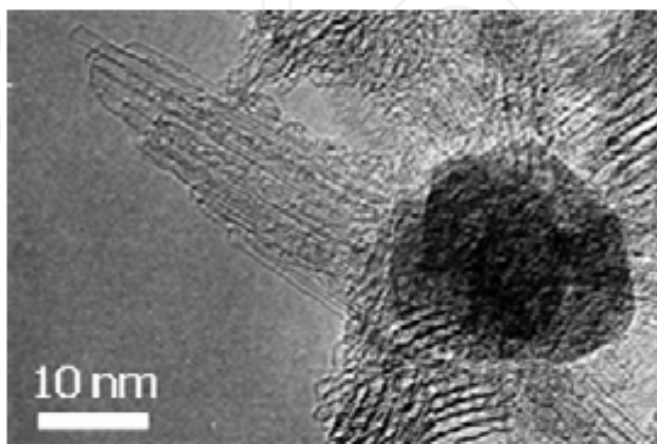

Fig. 13. TEM image of the product from graphite containing 20 at.% Y_2O_3 at Ar gas pressure of 0.1 MPa.

With increasing Ar gas pressure, the formation of C polyhedra filled with carbide particles was prominent. Figure 14 shows a TEM image of the product made from graphite containing 20 at.% Y_2O_3 at an Ar gas pressure of 0.2 MPa. Many carbide filled polyhedra are seen with sizes of 100–500 nm. Figure 15 shows a magnified TEM image and the corresponding SAED pattern of a polyhedron, indicating the formation of a PG particle having facets (Kokai et al., 2003) filled with a YC_2 crystallite particle according to JCPDS No. 11-0602. The diameters of the YC_2 particles were in the range of 30–150 nm. Compared to the diameters of the CNCs in hybridized SWCNH particles, larger YC_2 particles were included in the PG particle. The morphologies of the SWCNTs and PG particle are quite different from those of hybridized SWCNH particles.
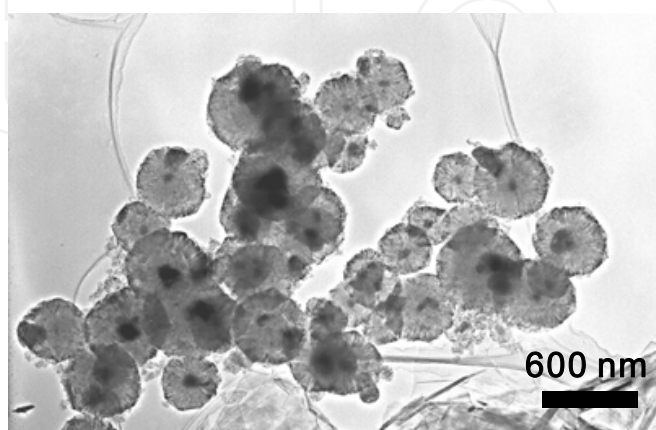

Fig. 14. TEM image of the product from graphite containing 20 at.% Y_2O_3 at Ar gas pressure of 0.2 MPa.
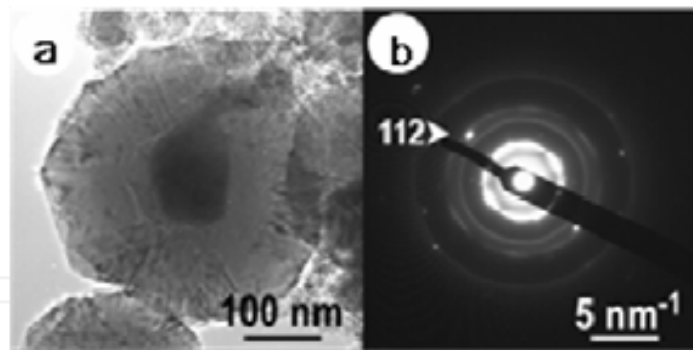
Fig. 15. (a) High-magnification TEM image and (b) the corresponding SAED pattern of the product from graphite containing 20 at.% Y_2O_3 at Ar gas pressure of 0.2 MPa.

The solubilities of C in liquid La and Y are very high, 42.9 and 70 at.%, respectively. The solubility of C in liquid Gd has not been reported, but Gd is known to form a carbide (GdC_2). Therefore, we believe that liquid-like molten metal-C particles are easily formed for these metals after laser ablation. For the growth of sea-urchin type SWCNTs under a relatively low Ar gas pressure condition, we believe that VLS growth, originally proposed to grow Si wires (Wagner & Ellis, 1964), play an important role through C dissolution, diffusion, and precipitation at the molten particles. The surface curvatures of the molten particles may change at the nucleation stage of SWCNTs, as reported from in situ observation of the dynamic deformation of metal particles resulting in a structure having a protrusion at the nucleation stage of a CNT (Hofmann et al., 2007; Yoshida et al., 2008). A SWCNT diameter may be determined by the size and shape of the highly curved structure at a molten particle that is saturated with C, resulting in a lift-off of a C cap to start the growth of a SWCNT. Unlike the SWCNTs grown efficiently from a graphite containing a small amount (~ 1 at.%) of Ni/Co as a catalyst (Guo et al., 1995; Yudasaka et al., 1997), the solubilities of C in liquid La, Gd, and Y, higher than those of Ni (2.7 at.%) and Co (4.2 at.%), are thought to govern the sea-urchin type SWCNT growth from a large (>20 nm) molten carbide particle.

For the formation of PG particles in laser ablation of pure graphite, high-temperature C species with a high resident density, established by confining C species with high-pressure Ar gas (0.5–0.9 MPa), are required (Kokai et al., 2004). In addition, PG particles were easily produced in the presence of 1 at.% Si or B in Ar gas, even at a low pressure of 0.1 MPa (Kokai et al., 2007). It was speculated that Si and B atoms could bind to a C atom and act as a seed to enhance the formation of C clusters. Similar to the behavior of Si and B atoms, carbide-filled PG particles in the presence of La, Gd, and Y may be grown by assembling C clusters around molten metal-C particles followed by graphitization at high-temperature in the range of 2000–3000 °C.

3.3 MWCNTs and BC-filled CNCs from graphite containing B₄C

Unlike laser ablation of graphite containing Fe, Co, and Ag, the laser ablation of graphite containing B_4C produced deposits containing MWCNTs with a high yield. The growth of MWCNTs was attempted by laser ablation combined with an electric furnace (Hirahara et al., 2000; Sabbaghzadeh et al., 2009); however, the dominant product was a CNC and the conditions for the nucleation and growth of MWCNTs by laser ablation are still not known well. Figure 16 shows typical SEM and TEM images of the deposit obtained by laser ablation

at a B content of 20 at.% in the target and at an Ar gas pressure of 0.1 MPa. In the SEM image (Fig. 16a), relatively straight 1D structures are seen together with particle-like products. Some of the 1D structures are up to 30 μm long. In the TEM images (Figs. 16b and 16c), the 1D structures are hollow MWCNTs. In the higher resolution TEM micrograph (Fig. 16c), a MWCNT with a 29 nm in diameter is observed. The MWCNT is composed of 31 graphitic layers with interlayer spacings of ~0.35 nm, indicating fairly good graphitization.

As seen in Figs. 16b and 16d, particle-like products, small graphitic C particles and boron carbide (BC) particles encapsulated in CNCs, were also generated together with the MWCNTs. However, hybridized SWCNH particles observed for Fe-, Co-, and Ag-containing targets, were not present in the deposit.
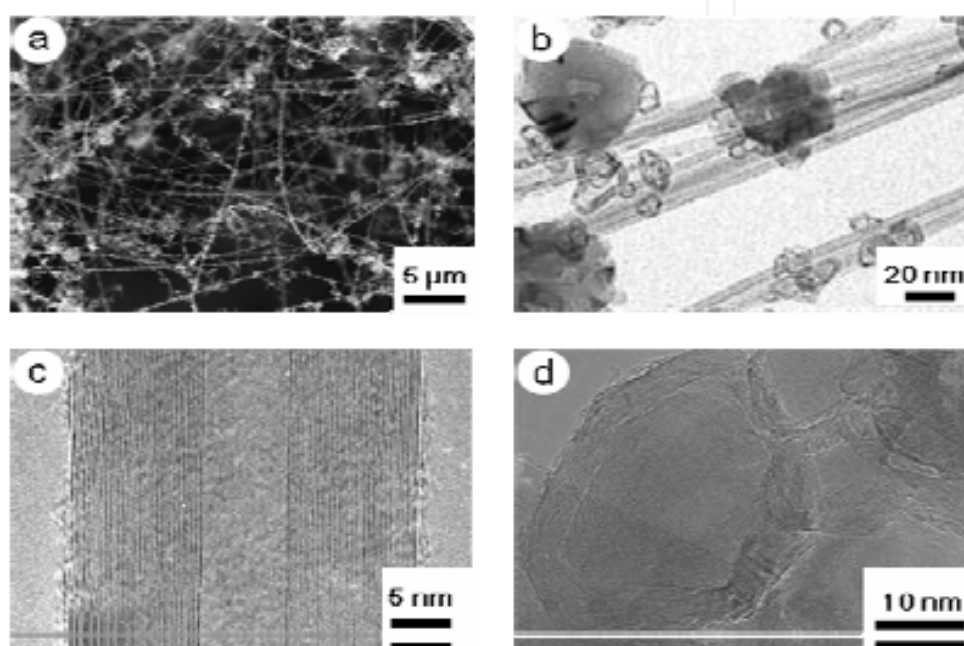

Fig. 16. (a) SEM and (b)TEM images of a deposit synthesized at B content of 20 at.% in the target and Ar gas pressure of 0.1 MPa. (c) Higher magnification TEM image of a MWCNT, 29 nm in diameter. (d) Higher magnification TEM image of CNCs filled with BC.

Further SEM and TEM studies on deposits produced by laser ablation under different conditions indicated that the fractions of MWCNTs in the deposits were highly sensitive to the B content in the graphite and the Ar gas pressure. The fractions of MWCNTs were roughly estimated by areas in TEM images for several parts in the deposit. Figure 17a shows the MWCNT fraction versus the B content. A constant Ar gas pressure of 0.1 MPa was used for the laser ablation. The MWCNT fraction is higher (50–60%) at B contents of 20–30 at.%. This fraction is much higher than previous studies using a nanosecond pulsed laser and an electric furnace (Hirahara et al., 2000; Sabbaghzadeh et al., 2009).

For the B contents lower and higher than 20–30 at.%, the MWCNT fraction decreased. In the lower B contents (1–10 at.%), small graphitic and PG particles were mainly produced. In the higher B contents (50–60 at.%), the major products were large BC-filled CNCs. Compared with the efficient growth of SWCNTs where the catalyst Ni/Co content in graphite is ~1 at.% (Guo et al., 1995; Yudasaka et al., 1997), the B content of 20–30 at.% in graphite for the optimum growth of MWCNTs is significantly different. Figure 17b shows the MWCNT fraction versus the Ar gas pressure. A constant B content of 20 at.% was used for the laser
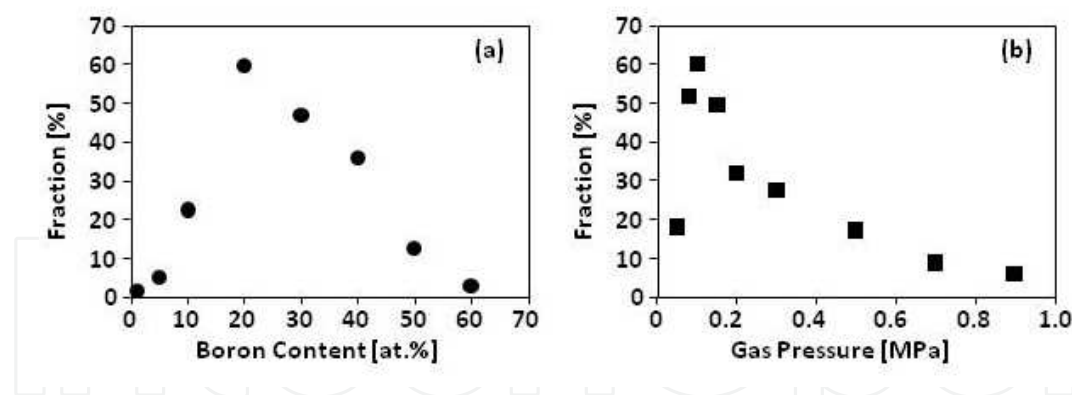
Fig. 17. Fractions of MWCNTs in the deposits versus (a) B content at Ar gas pressure of 0.1 MPa and (b) Ar gas pressure at B content of 20 at.%.

ablation. The MWCNT fraction shows a maximum (~60%) at 0.1 MPa. For Ar gas pressures lower and higher than 0.1 MPa, the MWCNT fraction decreases. At higher Ar gas pressures, large particles such as a PG particle and BC-filled CNCs, and thick rod-like whiskers were observed. At a low Ar gas pressure of 0.05 MPa, the major product was AC particles. The optimum Ar gas pressure of 0.1 MPa for the MWCNT growth is slightly higher than that of 0.07–0.08 MPa for the SWCNT growth (Guo et al., 1995; Yudasaka et al., 1997). We measured the diameters of more than 150 MWCNTs under each laser ablation condition. The diameter of the grown MWCNTs ranged from 7 to 70 nm.

Similar to previous observations (Hirahara et al., 2000), the presence of two types of BC particles, one encapsulated in CNCs (Fig. 16d) and another at a tips of MWCNTs, was confirmed in the present study. Figure 18a shows a TEM image showing a spherical BC particle about 39 nm in diameter at a tip of a MWCNT. In addition to the spherical BC particle, BC particles with various shapes such as ellipsoidal and elongated ones were observed as shown in Fig. 18b. Figure 18c shows a high-magnification TEM image of the portion of a BC particle surrounded by graphitic layers. Lattice fringes with spacings of 0.23 and 0.37 nm were observed and assigned to the distances between (021) and (012) planes in the B_4C crystal on the basis of the data of JCPDS No. 6-0555. The corresponding SAED pattern consists of two types: annular rings from surrounding graphene layers and spots from the BC core. Spots assigned to the (012) and (021) reflections of the B_4C crystal are seen. On the other hand, Figure 18d shows a high-magnification TEM image of a BC particle encapsulated in a CNC, where lattice fringes with spacings of 0.23 and 0.37 nm were also observed.

The diameter distributions of the two types of BC particles were compared (Hirahara et al., 2000). The diameters of the BC particles at MWCNT tips were 1–8 nm, while those of the BC particles in CNCs were 2–23 nm. As a result, they concluded that smaller BC particles seemed to be indispensable for the tubular growth and their critical diameter was found to be ~5 nm. In the present study, a similar tendency in diameters for the formation of MWCNTs and CNCs was observed in the two types of BC particles. Figure 19 shows diameter distributions of the two types of BC particles obtained for laser ablation at an Ar gas pressure of 0.1 MPa and a B content of 20 at.%. The diameters of BC particles at MWCNT tips and in CNCs are 10–100 nm and 20–280 nm, respectively. In this study, BC particles much larger than those of 1–8 nm seem to contribute to the growth of MWCNTs with large diameters up to 70 nm.
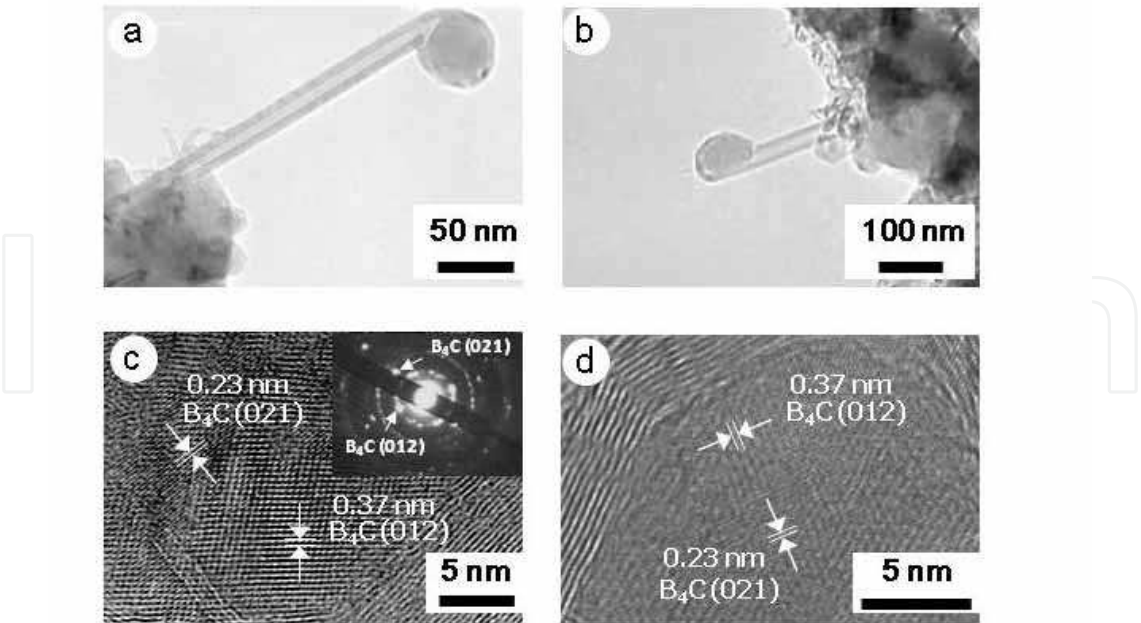
Fig. 18. (a, b) Low-magnification TEM images of the tips of MWCNTs with encapsulated BC particles. (c) High-magnification TEM image of portion of an encapsulated BC particle. The inset in (c) is the corresponding SAED pattern. (d) High-magnification TEM image of portion of an encapsulated BC particle in a CNC.
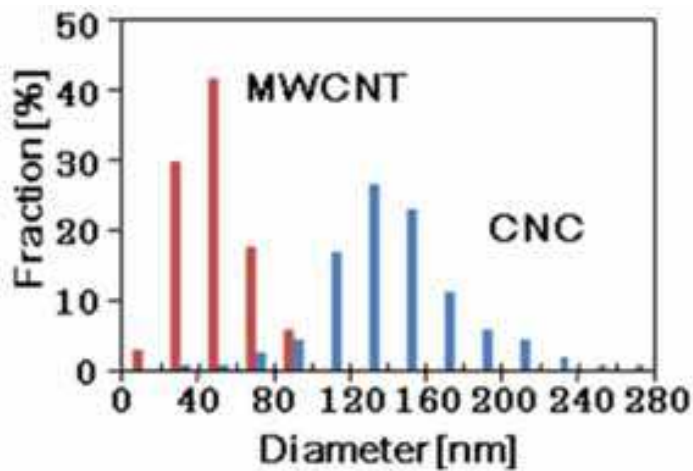

Fig. 19. Diameter distributions of two types of BC particles at tips of MWCNTs and in CNCs obtained from laser ablation at Ar gas pressure of 0.1 MPa and B content of 20 at.%.

As previously proposed (Hirahara et al., 2000), a B (in the form of BC) catalyzed growth mechanism of MWCNTs is considered because MWCNT tips encapsulating BC particles were also observed in the present study. However, much larger molten BC particles (10–100 nm) are thought to act as seeds at high temperature to grow MWCNTs that have up to 80 graphitic walls. The sizes of the catalyst particles were found to be crucial in terms of controlling the diameters and wall numbers to synthesize SW and MWCNTs in thermal chemical vapor deposition (Cheung et al., 2002). Other research groups have made similar observations (Li et al., 2001; Nerushev et al., 2003; Rümmeli et al., 2007). In the present laser ablation synthesis of MWCNTs, the B content in the graphite target and resident densities of laser-ablated B and C species confined by ambient Ar gas play an important role in

determining the size of molten BC particles. Unlike the thin SWCNT grown efficiently from a graphite target containing ~1 at.% Ni/Co, the observed optimum B amount of 20–30 at.% in the target (Fig. 17a) is consistent with the growth of MWCNTs with large diameters.

The VLS mechanism is thought to play a role in the growth of these MWCNTs, similar to the sea-urchin type SWCNTs in Section 3.2. The VLS growth of MWCNTs consists mainly of a three-part process: C is dissolved into a molten BC particle, diffused through the bulk and/or surface of the particle, and precipitated from the particle. According to the binary phase diagrams (Massalski et al., 1990), B has an eutectic temperature of 2375°C, which is much higher than those of Ni (1326.5°C) and Co (1320°C). B also has a C solubility (24.3 at.%) higher than those of Ni (2.7 at.%) and Co (4.2 at.%). Therefore, MWCNTs, which accompany the precipitation of large amounts of C are thought to be grown efficiently on large molten BC particles at temperatures higher than that (800–1300°C) for SWCNTs (Gorbunov et al., 1999). Although the actual temperature needed for C precipitation to form MWCNTs is not clear, temperatures up to ~2400°C may create favorable conditions for efficient MWCNT growth. Various shapes of BC particles observed in MWCNT tips such as spherical and elongated particles suggest that the surface curvatures of molten BC particles changes at the nucleation stage of MWCNTs as reported from in situ observation of the dynamic deformation of metal particles (Hofmann et al., 2007; Yoshida et al., 2008). A MWCNT diameter may be precisely determined by the size and shape of the highly curved structure resulting in a lift-off of a C cap.

Compared with the sizes of the two types of BC particles observed previously (Hirahara et al., 2000), much larger BC particles (10–280 nm) were observed at tips of MWCNTs (10–100 nm) and in CNCs (60–280 nm) in the present study (Fig. 19). In addition to the importance of the size of the molten BC particle for tubular growth (Hirahara et al., 2000), successive occurrence of the C dissolution-diffusion-precipitation process suitable for molten BC particles with specific sizes is thought to be indispensable for tubular growth. The growth of MWCNTs up to 70 nm in diameter may be governed by the action of molten BC particles with specific sizes. In addition to the B content in the target, the ambient Ar gas pressure also influence determining the sizes of BC particles. The C supply to the BC particles and its successive diffusion and precipitation are also influenced by Ar gas pressure, resulting in varying yields, diameters, and lengths of MWCNTs. Since larger molten BC particles could maintain C during the C supply, CNCs may form due to C not being precipitated at the high temperatures effective for the MWCNT growth. The formation of MWCNTs and CNCs is thought to relate to the balance among complex factors such as the resident densities of C and B species, C solubility in B particles, and the rates of C dissolution, diffusion, and precipitation. To form CNCs, C precipitation from core BC particles is believed to occur at the temperature lower than those to grow MWCNTs.

3.4 Cu-filled CNTs and CNCs from graphite containing Cu

Depending on the Ar gas pressure and Cu content, the deposits showing different morphologies were obtained (Kokai at al., 2009a). Figure 20 shows typical SEM images of deposits obtained at Ar gas pressures of 0.1, 0.5, and 0.9 MPa. Graphite targets with a constant Cu content of 20 at.% were used for laser ablation. As seen in Fig. 20a, sphere like particles with diameters of 30–130 nm were dominant at lower pressure regions of Ar gas (0.1–0.3 MPa). With increasing Ar gas pressure up to 0.9 MPa, the size of the particles was increased and the deposits became to contain straight 1D structures in addition to the sphere like particles (Figs. 20b and 20c).
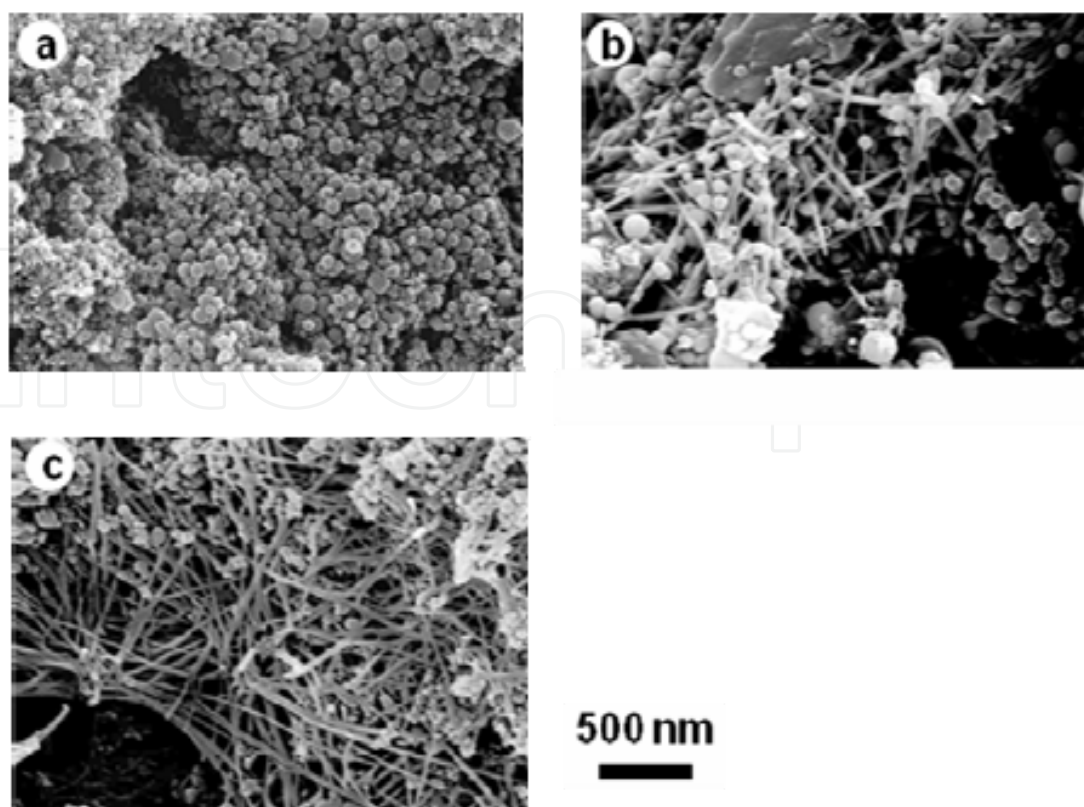
Fig. 20. SEM images of deposits produced at Ar gas pressures of (a) 0.1, (b) 0.5, and (c) 0.9 MPa.

TEM observation indicated that the sphere like particle obtained at lower Ar gas pressures were mainly composed of AC and SWCNH particles. Both particles include CNCs filled with Cu like the products shown in Section 3.1. Figure 21a is a typical TEM image of SWCNH particles, revealing diameters of 80−150 nm, including Cu-filled CNCs (dark areas). Figure 21b shows a TEM image observed near a core Cu particle of a SWCNH particle. Two graphitic layers with an interlayer spacing of about 0.34 nm are seen around the Cu particle as indicated by an arrow. The fraction of the hybridized SWCNH particles was ~70% at an Ar gas pressure of 0.2 MPa and with a Cu content of 20 at.% in the target.
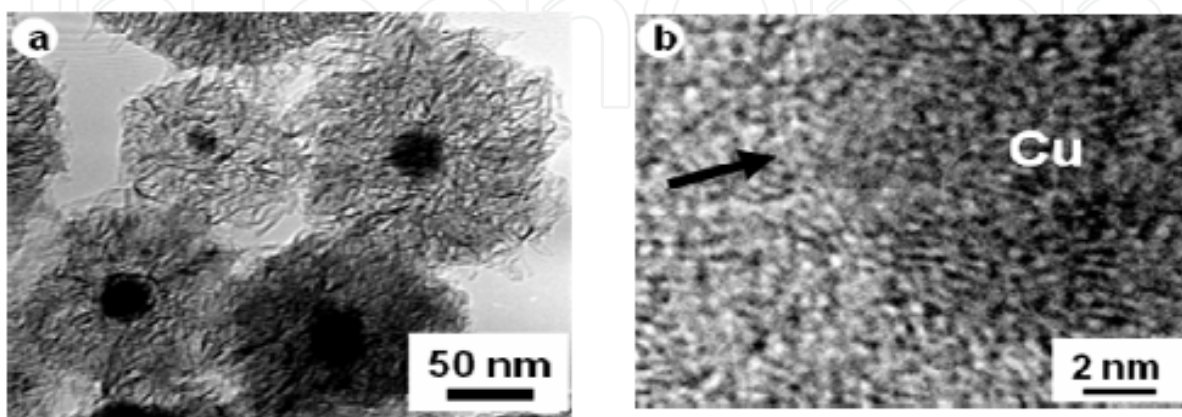

Fig. 21. (a) TEM image of SWCNH particles including Cu-filled CNCs. (b) High-magnification TEM image observed near the core Cu particle in a SWCNH particle.

Figure 22a is a typical TEM image of the deposit obtained at an Ar gas pressure of 0.9 MPa, which consists of 1D structures and sphere like particles. As seen in Fig. 22b, high-magnification TEM images of the 1D structures showed composite structures consisting of Cu nanowires with diameters of 18–20 nm surrounded by graphitic layers. The interlayer spacing in the graphitic layers is in the range 0.34–0.35 nm, which is slightly larger than that of graphite. Cu nanowires with up to seven graphitic layers were observed and Cu nanowires with 1–3 graphitic layers were dominant. Unlike previous studies using arc discharge, thermal chemical vapor deposition, and so on (Setlur et al., 1996; Zhang et al., 2003; Tao et al., 2006; Haase et al., 2007), in which both filled and unfilled CNTs were observed in deposited samples, in the TEM observation of more than 300 Cu-filled CNTs, unfilled or intermittently filled CNTs were not observed and all the grown CNTs contained Cu from root to tip.
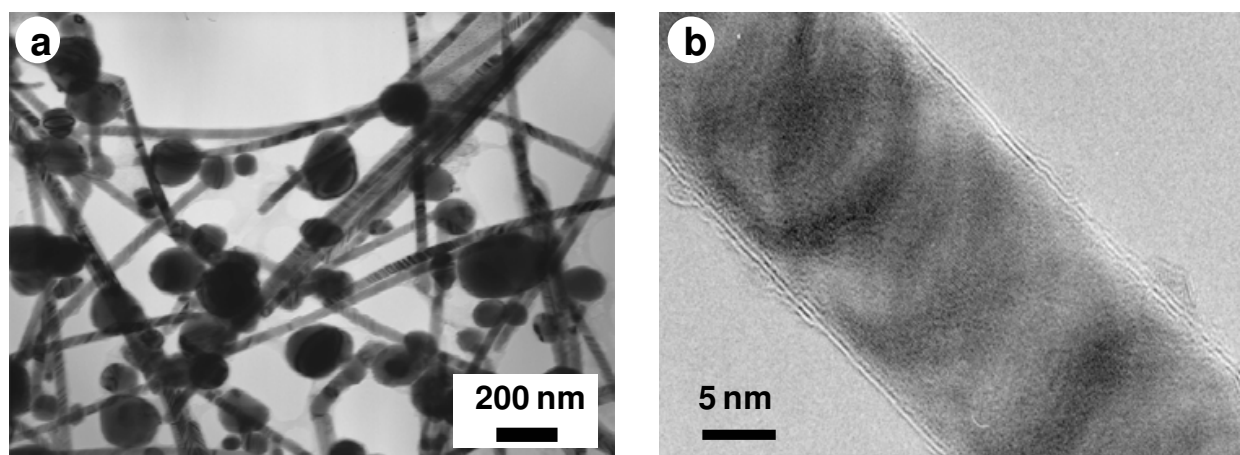

Fig. 22. (a) TEM image of a deposit obtained at Ar gas pressure of 0.9 MPa. (b) High-magnification TEM image of 1D structure with two graphitic layers.

Further characterization of the encapsulated Cu nanowire was carried out by the measurements of a high magnification TEM image and a SAED pattern (Fig. 23). According to JCPDS No. 4-0836, in the TEM image of a Cu wire, lattice fringes with spacing of 0.21 nm are seen corresponding to the distance of the Cu (111) planes. Also, in the SAED pattern, reflections assigned to graphite (002) and Cu (111), (200), and (220) planes are observed. These observed characteristics indicate the encapsulated Cu nanowire forms a polycrystal with a fcc structure. The fcc structure is predicted for a Cu nanowire encapsulated in a CNT by a theoretical study (Choi et al., 2003).

TEM examination of outer regions of the sphere like particles formed together with Cu-filled CNTs indicated that the particles were Cu-filled CNCs (Fig. 24). Cu is known as an element, which is not easily encapsulated in CNCs compared to other metals such as Co and Ni (Seraphin et al., 1996). A few studies (Lin et al., 1994; Jiao & Seraphin, 1998; Athanassiou, et al., 2006) showed that Cu nanoparticles are coated by only 3−4 graphitic layers. The Cu-filled CNCs in our study showed 3−9 graphitic layers. Thin graphitic layers were continuously curved to form spherical shell structures (Fig. 24a). Some thicker graphitic layers had flat sides joined at angles of 130°−150° (Fig. 24b).

In addition to the Ar gas pressure, we found the Cu content in the graphite target was also crucial for growing Cu-filled CNTs. Deposits obtained at different Cu contents at a constant Ar gas pressure of 0.9 MPa were investigated by TEM. As seen in Fig. 25a, when Cu content
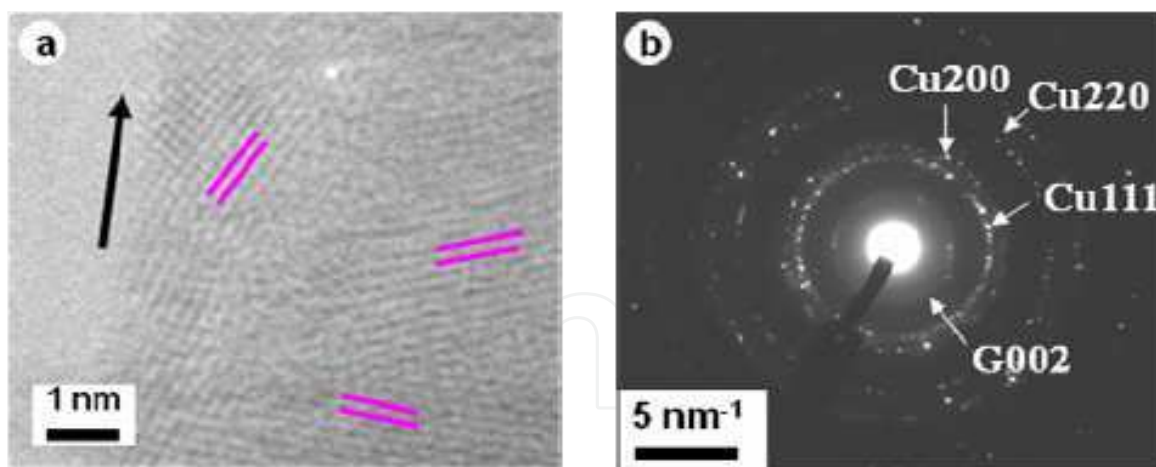
Fig. 23. (a) High magnification TEM image, focusing on the part of a Cu nanowire, and (b) its corresponding SAED pattern. In the TEM image, the arrow indicates the growth direction and the distance between the parallel fringes is close to the space of Cu (111) planes.
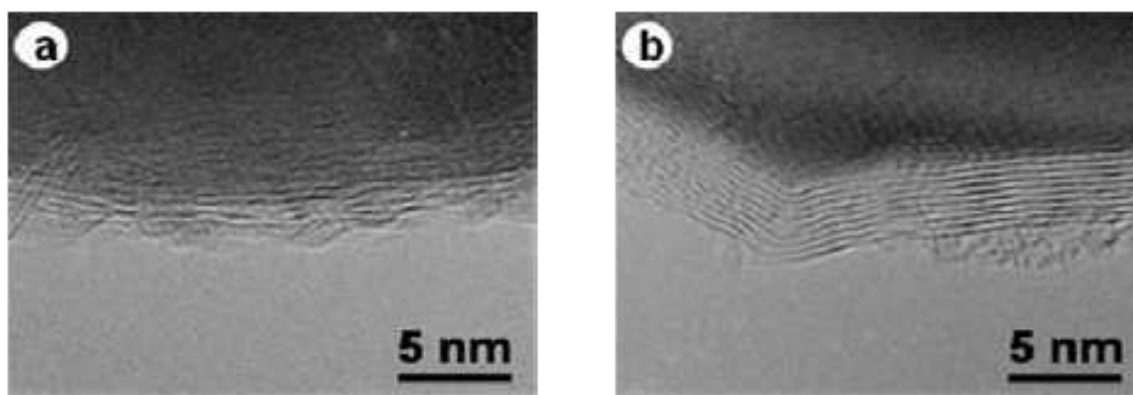

Fig. 24. TEM images of outer regions of CNCs with (a) thin and (b) thick graphitic layers.

was 1 at.%, Cu-filled CNTs were not formed and the major product was PG particles with diameters of 100–600 nm, similar to the product from the laser ablation of pure graphite (Kokai et al., 2003) and graphite containing 1 at.% Si or B (Kokai et al., 2007). With increasing the Cu content, Cu-filled CNTs were formed together with Cu-filled CNC with diameters of 10−120 nm (Fig. 25b). The yield of Cu-filled CNTs became a maximum around 20-30 at.% of the Cu content as shown in Fig. 22a. However, further increase in the Cu content led to a decrease in the yield of Cu-filled CNTs and the major products were Cu-filled CNCs. It is a unique feature that no unfilled CNT is seen even for low Cu content and all the grown CNTs contain Cu nanowires.

An interesting morphological feature of the Cu-filled CNTs in this work is that the diameter distribution is extremely narrow. The histogram shown in Fig. 26 is the diameter distribution of Cu-filled CNTs obtained from TEM images taken for more than 300 Cu-filled CNTs. The Cu-filled CNTs show uniform diameters ranging from 10 to 50 nm, and their mean diameter was calculated to be 19.8 nm. For comparison, the diameter distribution of Cu-filled CNCs is also shown in Fig. 26, and their diameters are 10–160 nm (59.7 nm mean diameter). The lengths of the Cu-filled CNTs ranged from 0.5 to 3 μm and their fraction was found to be approximately 60% in the total deposit from SEM and TEM examination of the deposit produced by using a graphite containing 20 at.% Cu at an Ar gas pressure of 0.9 MPa.
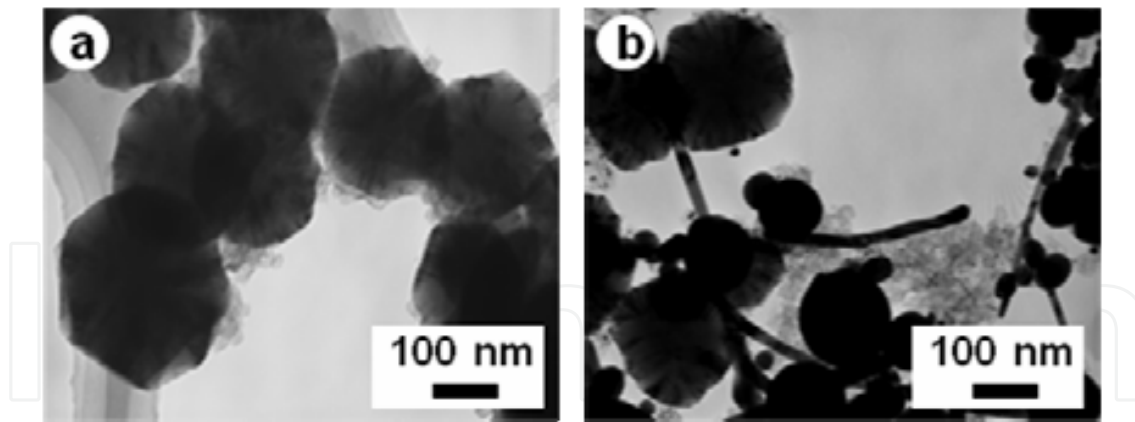
Fig. 25. TEM images of deposits obtained from graphite containing Cu of (a) 1 and (b) 5 at.%. A constant Ar gas pressure of 0.9 MPa was used.
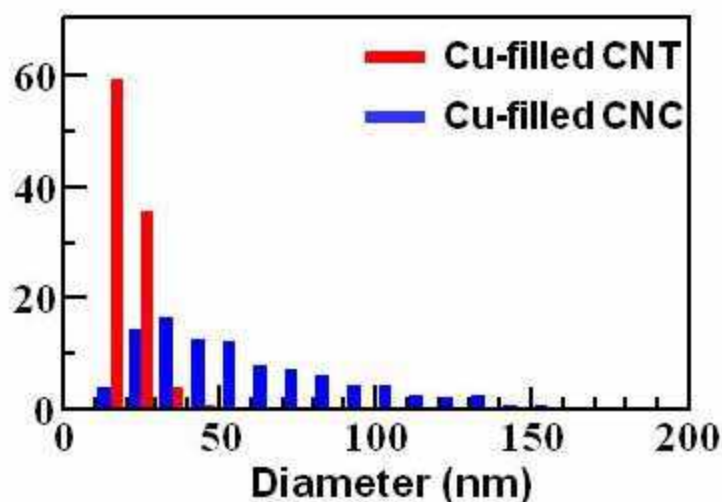

Fig. 26. Diameter distributions of Cu-filled CNTs and CNCs obtained for the deposit produced at Ar gas pressure of 0.9 MPa from graphite containing 20 at.% Cu.

To understand the possible growth mechanism for these unique Cu-filled CNTs, their edges were carefully examined by TEM. As shown in Fig. 27a, straight Cu-filled CNT structures, possessing sphere like particles at their edges, were observed. As seen in Fig. 27b, graphitic layers similar to those covering Cu nanowires were observed for the sphere like particles. The presence of the sphere like particles indicates the contribution of molten particles to form the Cu-filled CNTs. However, a well-known VLS mechanism (Wagner & Ellis, 1964) does not seem to act because of the absence of catalytic particles at the edges of the Cu-filled CNTs. In addition, formation mechanism of metal-filled CNT based on the growth of CNTs and simultaneous metal filling proposed for an arc discharge process (Demoncy et al., 1998) can not be applied because unfilled CNTs were not present.

CNTs completely filled with Cu nanowires are preferentially fabricated together with Cu-filled CNCs in a high pressure Ar gas environment of 0.9 MPa. In the space confined by Ar gas of high pressure such as 0.9 MPa, the collisions between C and Cu species are expected to be enhanced, although the exact size and feature of C and Cu species are not clear. We believe that strong interaction between C and Cu species results in the formation of molten Cu-C particles with unusually C-rich compositions at elevated temperature, while C interaction
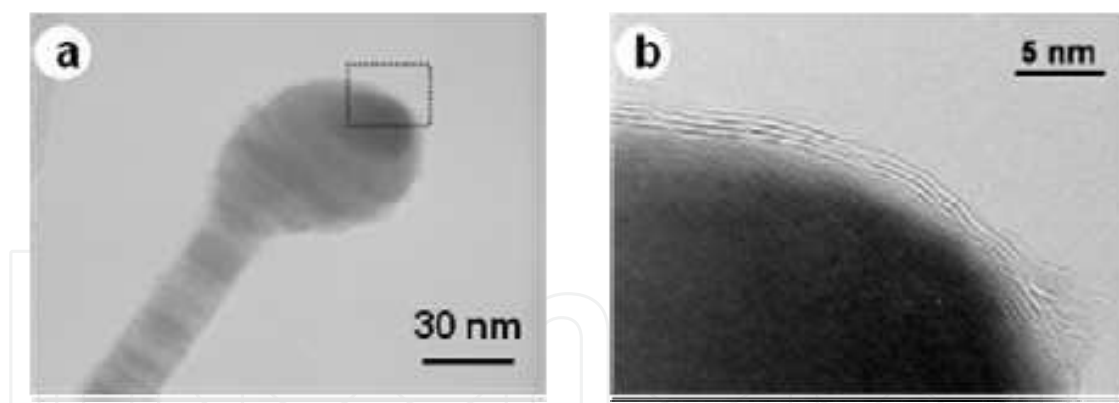
Fig. 27. (a) TEM image of a Cu-filled CNT with a spherical particle at its edge and (b) high magnification TEM image of outer region of the sphere like particle (rectangular area in Fig. 27a).

with Cu at normal atmospheric pressure is known to be weak (binding energy of 0.1–0.144 eV/atom (Seraphin et al., 1996; Tao et al., 2006)) and the C solubility is very low (0.04 at.%) (Massalski et al., 1990).

From the formation of Cu-filled CNTs together with CNCs including larger Cu particles and a narrow diameter distribution of Cu-filled CNTs (Fig. 26), we propose that molten Cu-C composite particles with certain small sizes play a crucial role in the formation of Cu-filled CNTs. The unusual composition of C and Cu, probably a C-rich one, in the molten particles and successive supply of C and Cu to the molten particles result in the precipitation of C and Cu. The growth of a Cu-C 1D composite structure followed by phase separation to form graphitic layers around the Cu nanowires finally leads to formation of Cu-filled CNTs. Escaping from unusually C-rich state for strain relaxation may be a driving force to precipitate C and Cu without the need of a catalyst.

3.5 SiC platelets and nanowires and SiC-filled MWCNTs from graphite containing Si

Deposits exhibiting particle and 1D structures with amorphous and crystalline features were observed for various Si content (5–70 at.%) and Ar gas pressure (0.05–0.9 MPa), instead of hybridized SWCNH particles. Figure 28 shows a typical TEM image of a deposit produced at an Si content of 20 at.% and an Ar gas pressure of 0.05 MPa. Sphere-like and irregular shaped amorphous particles with sizes of 5–150 nm are seen.
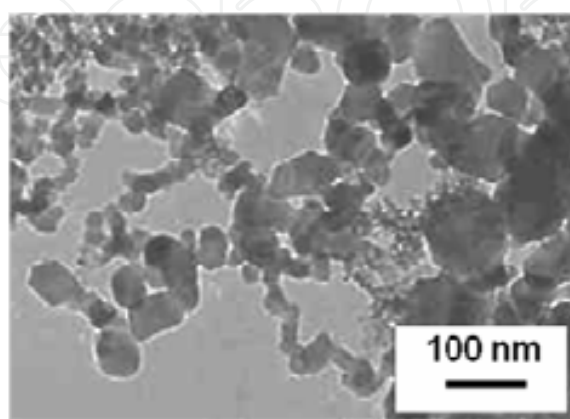

Fig. 28. TEM image of a deposit produced at Si content of 20 at.% and Ar gas pressure of 0.05 MPa.

An increased Si content resulted in platelet-like particles. Figure 29a shows a TEM image of a deposit produced at an Si content of 60 at.% and an Ar gas pressure of 0.05 MPa. Triangular and hexagonal platelet-like particles with sizes of 50–300 nm are seen together with sphere-like and irregular shaped particles. In the SEM image of the deposit as shown in Fig. 29b, cross sections of some platelets were observed and indicated the platelet thicknesses were in the range of 30–60 nm. The high-magnification TEM image of the platelet-like particle shown in Fig. 29c reveals lattice fringes of a spacing of 0.25 nm assigned to the (111) planes of cubic β-SiC based on the data of JCPDS No. 1-1119. The SAED also shows a typical pattern of the β-SiC phase consisting of spots forming a hexagon. These results suggest that the {111} crystal plane is the basal plane.
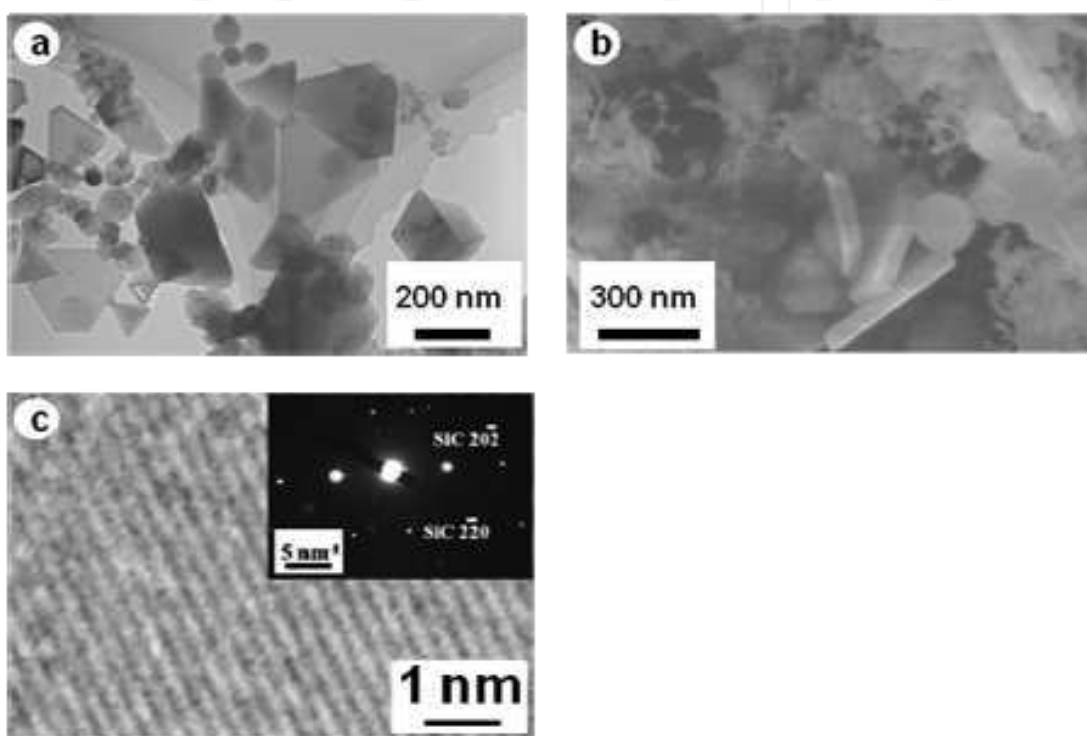

Fig. 29. (a) TEM and (b) SEM images of a deposit produced at Si content of 60 at.% and Ar gas pressure of 0.05 MPa and (c) higher magnification TEM image of a platelet particle. The inset in (c) is the corresponding SAED pattern.

Figure 30a shows a Raman spectrum of the deposit containing the platelet-like particles. Figure 30b shows the Raman spectrum in the 750–850 cm^{-1} region of Fig. 30a in the enlarged scale. Three peaks are seen at 520, 789, and 970 cm^{-1}. From previous Raman spectroscopic studies of SiC films (Chehaidar et al., 2001; Hu et al., 2004; Xu et al., 2005), the two weak bands at 789 and 970 cm^{-1} are assigned to those due to transverse and longitudinal optical phonon modes of SiC. However, the strong band observed at 520 cm^{-1} is attributed to an Si-Si transverse optical phonon mode. The weak band observed at 970 cm^{-1} is probably overlapped with a band due to the second order Si-Si longitudinal optical phonon mode. These results lead us to believe that nanoparticles of Si and/or Si-rich SiC exist in addition to crystalline SiC platelets in the deposit, while the scattering intensity of the Si-Si band at 520 cm^{-1} relative to that of the SiC band at 789 cm^{-1} is much higher. Similar hexagonal crystalline SiC platelets were synthesized using an autoclave heated at 350–500 °C for 20–40 h (Ju et al., 2009). The formation of hexagonal platelets was thought to be due to the

preferential development of {111} and {110} planes of crystalline SiC. We believe that a similar development of {111} and {110} planes is involved in the growth of triangular and hexagonal SiC platelets by assembling a suitable amount of Si and C species after laser ablation.
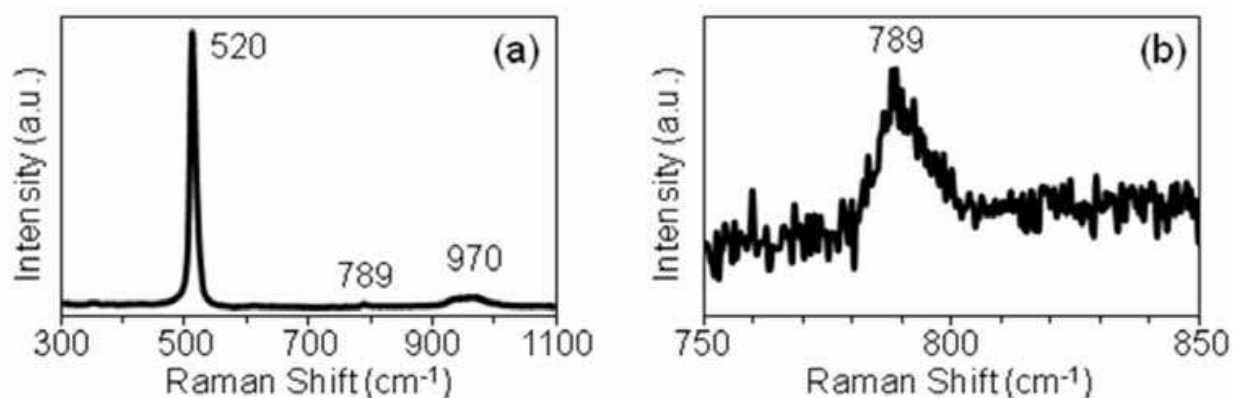

Fig. 30. (a) Raman spectrum of a deposit produced at Si content of 60 at.% and Ar gas pressure of 0.05 MPa. (b) Raman spectrum in the 750–850 cm^{-1} region of Fig. 30a in the enlarged scale.
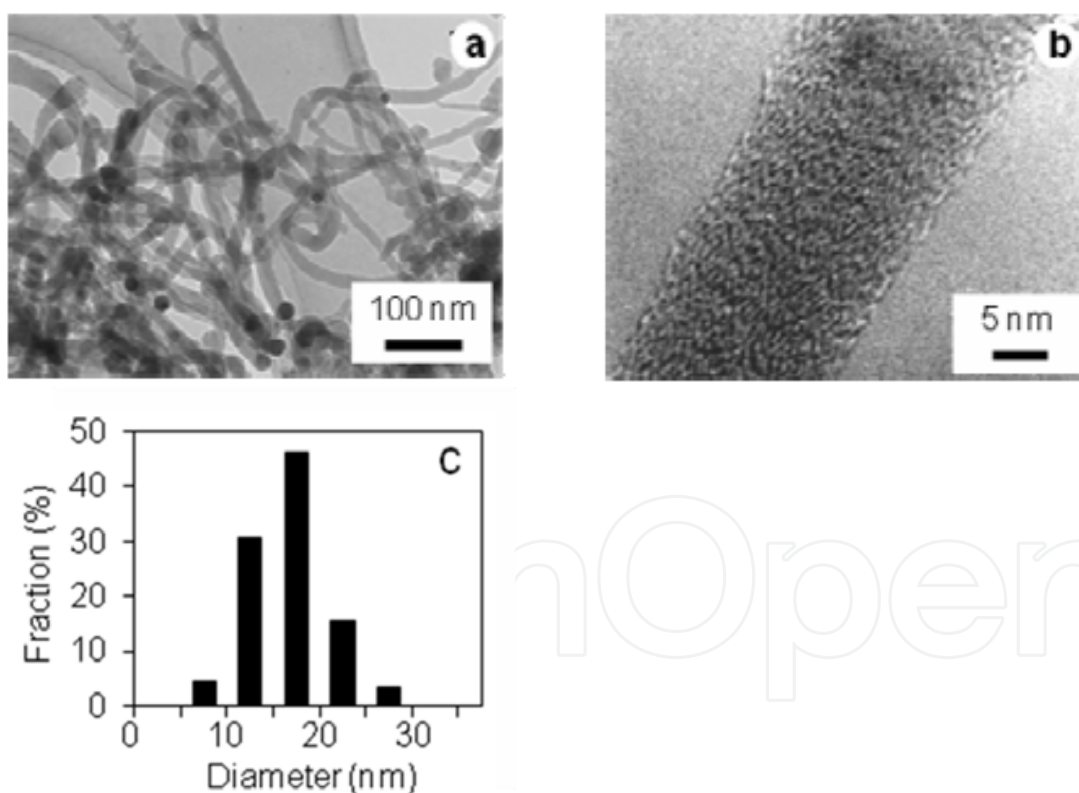

Fig. 31. TEM images of (a) thin 1D structures (amorphous nanowires) and (b) one amorphous nanowire produced at Si content of 70 at.% and Ar gas pressure of 0.1 MPa. (c) Distribution of diameters of amorphous nanowires.

Further increased Si content and Ar gas pressure resulted in 1D nanostructures with different thicknesses, lengths, and linearities (Kokai et al., in 2010). Using SEM, TEM, SAED, and Raman spectroscopy for the 1D nanostructures, we found that there were two types of

1D nanostructures: (1) an amorphous SiC nanowire and (2) a MWCNT filled with a crystalline SiC nanowire. Figure 31a shows a TEM image of the thin 1D nanostructures grown at an Si content of 70 at.% and an Ar gas pressure of 0.1 MPa. Curved nanowires can be observed. A further magnified TEM image (Fig. 31b) indicates an amorphous feature. Nanowires with diameters of 5–30 nm were observed. The diameter distribution obtained from the measurement of more than 200 samples is shown in Fig. 31c. Nearly 80% of the nanowires have diameters of 10–20 nm; the average diameter is 16 nm. The lengths of the nanowires were 0.5–2 μm from the observation of SEM images.

Figure 32 shows Raman spectra of the deposit including curved 1D nanostructures. Similar to the Raman spectra of Fig. 30, three peaks are seen at 520, 795, and 973 cm^{-1}. Compared to the intensity distribution in Fig. 30, the intensity of the band at 795 cm^{-1} relative to those of other two bands is decreased. Therefore we conclude the 1D nanostructure is an Si-rich amorphous SiC nanowire. The presence of the strong band at 520 cm^{-1} may indicate that nanowires composed of only Si are also included in the deposit.
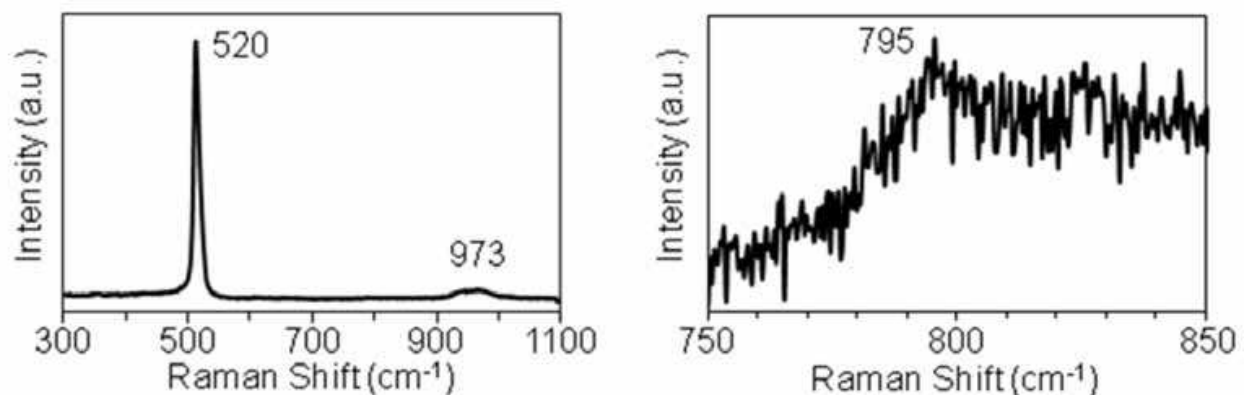

Fig. 32. (a) Raman spectra of a deposit including curved 1D nanostructures produced at Si content of 70 at.% and Ar gas pressure of 0.1 MPa. (b) Raman spectrum in the 750–850 cm^{-1} region of Fig. 32a in the enlarged scale.

With further increase of the Ar gas pressure, we found an increase in the amount of 1D nanostructures relative to the particles in the deposits. Figure 33a shows a typical TEM image of a deposit produced at an Si content of 70 at.% and an Ar gas pressure of 0.9 MPa. Straight and thick 1D nanostructures are seen. Figure 33b shows a higher-magnification TEM images of a 1D nanostructure. The different light and dark contrast observed in the 1D nanostructure indicates a coaxial structure of two different compositions. The TEM image of the outer portion seen in Fig. 33c indicates the presence of graphitic layers with an interlayer distance of ~0.35 nm. The TEM image focusing on the core seen in Fig. 33d exhibits lattice fringes of a spacing of 0.25 nm assigned to the (111) planes of cubic β-SiC as seen in Fig. 29c. The SAED also shows a typical pattern of the β-SiC phase. These results indicate the 1D nanostructure is a MWCNT filled with a crystalline SiC nanowire. The lengths of the SiC-filled MWCNTs were 2–20 μm from the observation of SEM images. Figure 34 shows two Raman spectra observed in two different Raman shift regions for a deposit including the straight and thick 1D nanostructures. Similar to the Raman spectra of Figs. 30 and 32, three bands are observed at 519, 789, and 969 cm^{-1} in the region of 300–1100 cm^{-1}. Like the typical Raman spectrum of MWCNTs synthesized using arc discharge and thermal chemical vapor deposition (Enomoto et al., 2006), two bands assigned to D and G bands are observed at 1356 and 1583 cm^{-1}, respectively.
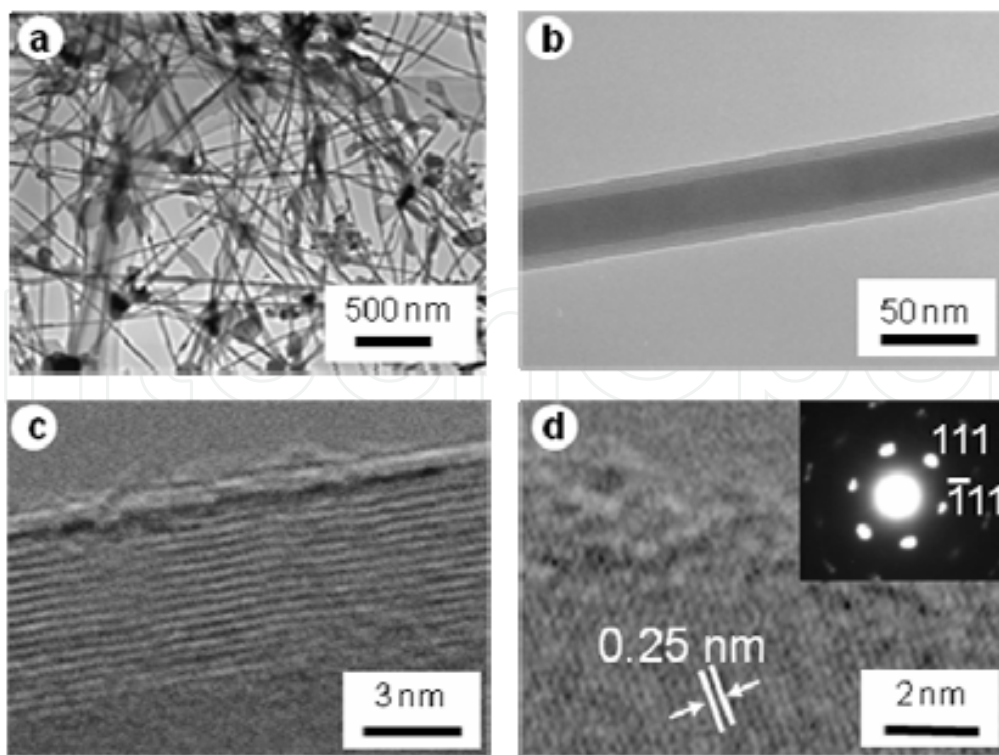
Fig. 33. (a) High-magnification TEM images of the 1D structure (crystalline SiC-filled MWCNT) produced at Si content of 70 at.% and Ar gas pressure of 0.9 MPa. (b) one 1D structure, (c) outer portion, and (d) lattice image of core SiC. The inset in (d) is the corresponding SAED pattern.
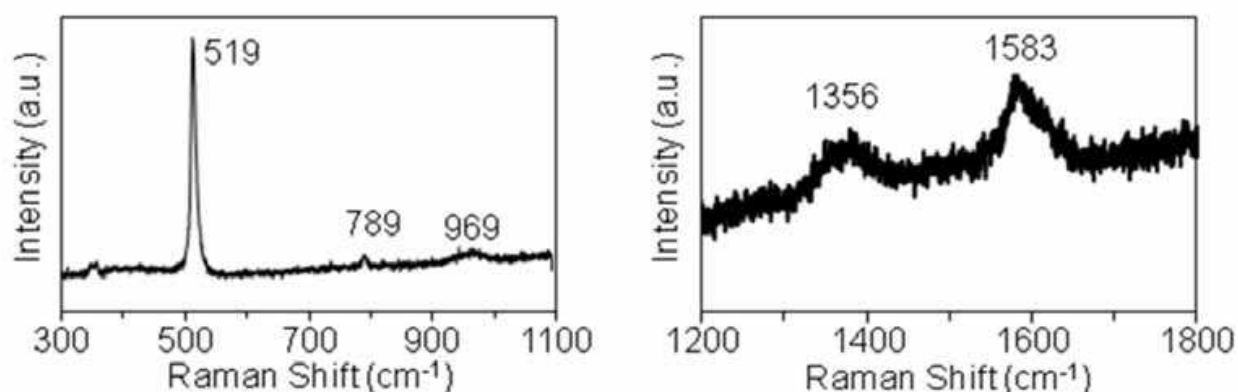

Fig. 34. Raman spectra of the deposit including the straight and thick 1D nanostructures observed in (a) 300–1100 and (b) 1200–1800 cm⁻¹.

A further detailed structure of the SiC-filled MWCNT was investigated by the measurement of the outer and SiC diameters of more than 200 SiC-filled MWCNTs. Figure 35a shows the distribution of the outer diameters of SiC-filled MWCNTs. The diameters range from 10 to 60 nm. More than 80% of the diameters are 20–40 nm; the average diameter is 32 nm. Figure 35b shows the distribution of the diameters of crystalline SiC nanowires encapsulated in MWCNTs. The diameters range from 15 to 50 nm, of which more than 80% of the diameters are 10–30 nm and the average diameter is 21 nm. These results indicate that the thicknesses of the graphitic layers of the MWCNTs are 2–9 nm (5–26 layers).

Unlike the thin amorphous SiC nanowires produced at an Ar gas pressure of 0.1 MPa, high Ar gas pressures of 0.5–0.9 MPa were essential for the formation of crystalline SiC-filled MWCNTs. The SiC-filled MWCNTs produced at low Si contents (30–50 at.%) were short and bending, probably due to the presence of defects. Increasing the Si content up to 70 at.%, enables the formation of straight and long SiC-filled MWCNTs. We checked more than 300 SiC-filled CNTs with TEM and found there were no MWCNTs without SiC filling from root to tip.
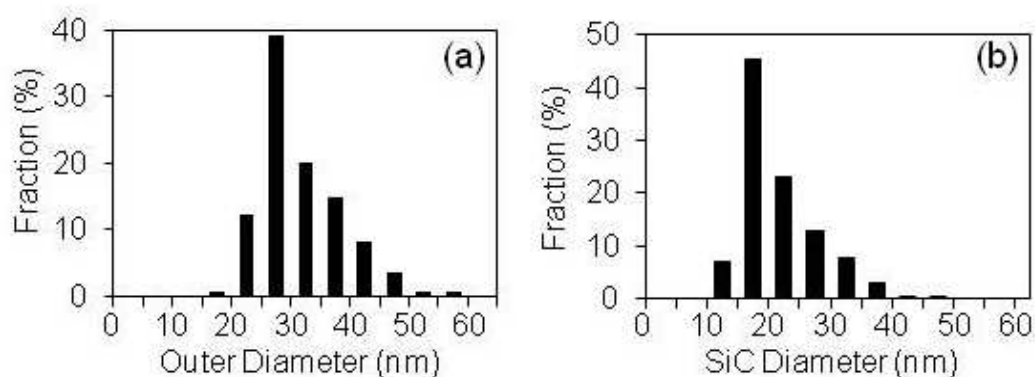

Fig. 35. Distributions of (a) outer diameters of SiC-filled MWCNTs and (b) diameters of the encapsulated SiC nanowires.

To understand the possible growth mechanisms for the two 1D nanostructures, their ends were carefully examined with TEM. For the amorphous SiC nanowires, sphere-like particles with uniform diameters of 25–30 nm were observed at their tips as shown in Fig. 36a. Some of the sphere-like particles are also seen in Fig. 31a as dark contrast portions. Figure 36b shows a high-magnification TEM image of a sphere-like particle, revealing that the sphere-like particle has an amorphous feature similar to the portion of the SiC nanowire as seen in Fig. 31b. On the other hand, for crystalline SiC-filled CNTs, angular polyhedron-like particles with sizes (100–400 nm) larger than the sphere-like particles were observed as shown in Figs. 36c and 36d. Figure 36e shows a high-magnification TEM image of the outer portion of a polyhedron-like particle, revealing that the particle is wrapped with graphitic layers as seen in the crystalline SiC-filled CNTs (Fig. 33c). The particle structure wrapped with graphitic layers at the tip is similar to that of the Cu-filled CNT in Section 3.4.

The presence of these sphere- and polyhedron-like particles indicates the contribution of liquid-like molten particles in the nucleation and continuous growth of the two 1D nanostructures. Similar to Cu-filled CNTs, catalyst materials are not present at the tips. When we used a Si powder of 99.999% purity instead of a 99% purity Si powder for laser-irradiation targets, same two types of 1D structures were formed. We measured x-ray photoelecton spectra of the deposits containing two 1D structures and detected Si, C, and O elements. However, other elements were not detected within the detection limit of 0.1 at.%. Therefore, the conventional VLS mechanism can not be applied for the growth of the two 1D nanostructures. Furthermore, an oxide-assisted growth mechanism (Zhang et al., 2003), proposed for Si and other nanowires together with the observation of oxide cover layers, and the conversion of CNTs to SiC nanowires (Dai et al., 1995: Ye et al., 2005) do not seem to contribute to the growth of these two 1D structures. We speculate that the somewhat different driving forces that nucleate the two 1D nanostructures are induced in the Si-containing molten particles without a catalyst. The yields and linearity of the two 1D nanostructures
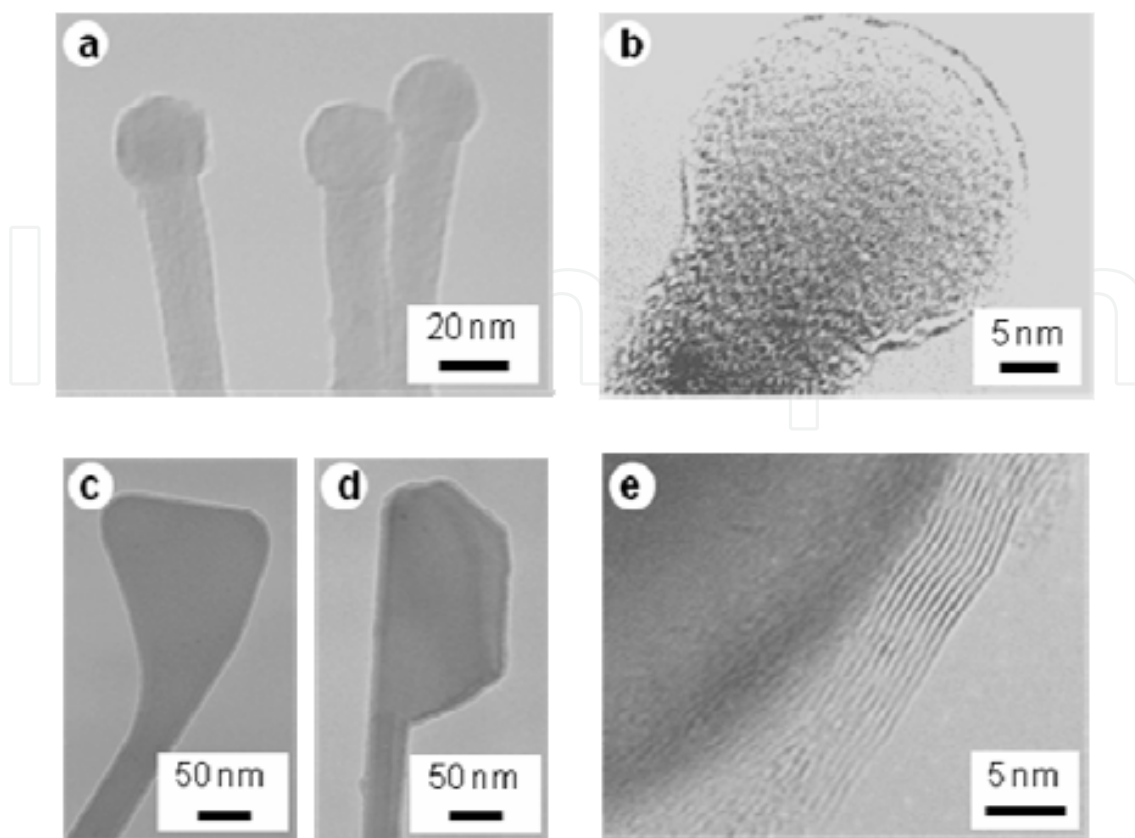
Fig. 36. Typical TEM images of the tips of (a, b) amorphous SiC nanowires and (c, d) crystalline SiC-filled CNTs. (e) TEM image of outer region of the tip of crystalline SiC-filled CNT

were strongly dependent on the compositions of Si and C in the laser-irradiation targets and Ar gas pressure. Therefore, Si-C molten particles with specific compositions, governed by the resident densities and temperatures of Si and C and their supply to the Si-C molten particles are thought to self-catalytically contribute the precipitation of Si and C to form the 1D nanostructures. We suggest that the instability of molten Si-C particles occurred together with the successive supplies of Si and C and resulted in Si and C precipitation. Silicon-rich molten particles may contribute to the formation of amorphous SiC nanowires as proposed in the formation of submicrometer SiC whiskers by the carbothermal reduction of silica at ~1500°C (Belmonte et al., 1996). Compared to the formation of amorphous SiC nanowires, ablated C and Si species with higher resident densities contribute to the growth of crystalline SiC-filled CNTs over a longer time at high temperature due to the stronger confinement of ablated Si and C, like the formation of PG particles and Cu-filled CNTs. This may result in the growth of a Si-C nanostructure followed by phase separation to form the outer graphitic layers. From the shapes of the tips and the grown SiC-filled CNTs in Figs. 36c and 36d, the deformation of the molten particles (formation of protrusion-like structures), as reported in-situ TEM images for the formation of CNTs (Hofmann et al., 2007; Yoshida et al., 2008), may be involved in the nucleation of Si-C nanostructures. The graphitic-layer-covered polyhedron-like shapes of the tips formed after growth of the SiC-filled CNTs probably results from the formation of crystalline SiC with facets of 50–300 nm.

4. Conclusion

We have presented a simple method to form various nanocarbon and composite structures using laser ablation in high-pressure Ar gas up to 0.9 MPa. Graphite containing Si, Fe, Co, Ni, Cu, Ag, B_4C, La_2O_3, Gd_2O_3, or Y_2O_3 was used as a source material. The laser ablation of graphite containing Fe, Co, Ni, and Ag enabled the high yield (~70%) fabrication of hybridized SWCNH particles including metal- or carbide-containing CNCs. Other by-products such as CNCs and hybridized PLG particles were also observed. For La_2O_3, Gd_2O_3, and Y_2O_3, hybridized SWCNH particles were not observed. Instead, products such as sea-urchin-type SWCNTs and PG particles including carbide particles were formed. Unlike the addition of these metals and compounds to graphite, different products were observed for B_4C, Cu, and Si by adjusting the Ar gas pressure and additive content. For B_4C, in addition to CNCs containing BC, MWCNTs were grown with a high yield of ~60%. For Cu, in addition to hybridized SWCNH particles including Cu-containing CNCs, CNTs filled with polycrystalline Cu nanowires were formed. For Si, three characteristic Si-C nanostructures, i.e., SiC platelets, amorphous SiC nanowires, and CNTs filled with crystalline SiC nanowires, were formed. Unlike previous work on the formation of CNTs filled with metals and compounds, the present method involves a high-pressure Ar gas of 0.9 MPa and has a unique feature in that all the grown CNTs contained Cu or SiC nanowires and no empty CNTs were present in the deposits. We have discussed the metal-dependent efficient growth of various nanocarbon and composite structures from high-temperature C and metal species confined by Ar gas. The co-existence of SWCNHs formed by thermal graphitization and smaller molten C-metal particles is probably essential to the formation of hybridized SWCNH particles; otherwise, the formation of CNCs and other structures are promoted. The strong correlation between the hybrid diameter and SWCNH layer thickness for Fe, Co, and Ag hybrids suggests that after SWCNHs with a certain range of lengths are formed, they aggregate around molten metal-C particles with a certain range of diameters. The C precipitation by catalytic graphitization, which leads to the formation of CNCs in SWCNH aggregates, occurs after SWCNH assembly. The VLS mechanism is thought to play a role in the growth of sea-urchin type SWCNTs and MWCNTs through C dissolution, diffusion, and precipitation. The nanostructures (diameters and wall numbers) of the SW and MWCNTs may be precisely determined by the sizes and shapes of the highly curved structures at molten C-catalyst particle, which results in lift-offs of C caps. The B-catalyzed MWCNT and CNC formation is thought to relate to the balance among complex factors such as resident densities of C and B species, C solubility in B particles, and rates of C dissolution, diffusion, and precipitation. The presence of sphere- and polyhedron-like particles at the tips of grown 1D nanostructures of Cu-filled CNTs, SiC nanowires, and SiC-filled CNTs indicates the contribution of liquid-like molten particles in the nucleation and continuous growth of these 1D nanostructures. A catalyst-free unconventional VLS mechanism, in which self-catalytic action in molten Cu-C and Si-C particles that is dependent on their compositions may be involved, plays a significant role in the growth of the 1D nanostructures. Although the details of the growth mechanisms proposed here are not clear, we believe that the present method using a high-pressure gas atmosphere can be extended to the growth of nanowires of other metal and semiconducting materials. Applications such as drug delivery, catalyst supports, spot welding, thermal management, and structural devices are expected in the future by using such nanocarbon and composite materials.
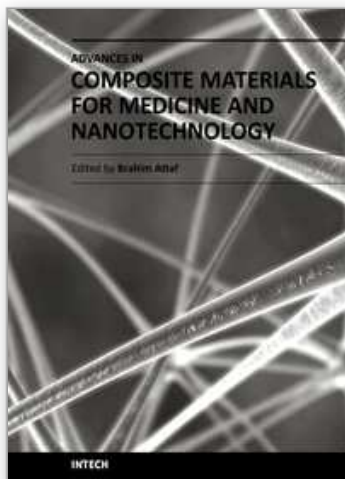
5. Acknowledgements

6. References

Athanassiou, E.K.; Grass, R.N. & Stark, W.J. (2006). Large–scale production of carbon-coated copper nanoparticles for sensor applications, *Nanotechnology*, *17*, 1668–1673, 0957-4484

Belmonte, T.; Bonnetain, L. & Ginoux, J.L. (1996). Synthesis of silicon carbide whiskers using the vapour-liquid-solid mechanism in a silicon–rich droplet, *J Mater. Sci.*, 31, 2367–2371, 0022-2461

Chehaidar, A.; Zwick, A. & Carles, R. (2001). Investigation of structural and chemical ordering in Si-rich amorphous SiC alloys via Raman spectroscopy and numerical modelling, *J Phys., Condens. Matter*, 13, 10743 –10755, 0953-8984

Cheng, M.-D., Lee, D.-W.; Zhao, B.; Hu, H.; Styers-Barnett, D.J.; Puretzky, A.A.; DePaoli, D.W.; Geohegan, D.B.; Ford, E.A. & Angelini, P. (2007). Formation studies and controlled production of carbon nanohorns using continuous in situ characterization techniques, *Nanotechnology*, 18, 185604 (8p), 0957-4484

Cheung, C.L.; Kurtz, A.; Park, H. & Lieber, C.M. (2002). Diameter-controlled synthesis of carbon nanotubes, *J Phys. Chem. B*, 106, 2429–2433, 1520-6106

Choi, W.Y.; Kang, J.W. & Hwang, H.J. (2003). Structures of ultrathin copper nanowires encapsulated in carbon nanotubes, *Phys. Rev. B*, 68, 193405-1–193405-4, 0163-1829

Dai, H.; Wong, E.W.; Lu, Y.Z.; Fan, S. & Lieber, C.M. (1995). Synthesis and characterization of carbide nanorods, *Nature*, 375, 769–772, 0028-0836

Demoncy, N.; Stéphan, O.; Brun, N. ; Colliex, C. ; Loiseau, A. & Pascard, H. (1996). Filling carbon nanotubes with metals by the arc-discharge method: the key role of sulfur, *Eur. Phys. J B*, 4, 147–157, 1434-6028

Enomoto, K.; Kitakata, S.; Yasuhara, T.; Ohtake, N.; Kuzumaki, T. & Mitsuda, Y. (2006). Measurement of Young's modulus of carbon nanotubes by nanoprobe manipulation in a transmission electron microscopy, *Appl. Phys. Lett.*, 88, 153115 (3p), 0003-6951

Gorbunov, A.A.; Friedlein, R.; Jost, O.; Golden, M.S.; Fink, J. & Pompe, W. (1999). Gas-dynamic consideration of the laser evaporation synthesis of single-wall carbon nanotubes, *Appl. Phys. A*, 69, S593–S596, 0947-8396

Guo, T.; Nikolaev, P.; Thess, A.; Colbert, D.T. & Smalley, R.E. (1995). Catalytic growth of single-walled nanotubes by laser vaporization, *Chem. Phys. Lett.*, 243, 49–54, 0009-2614

Haase, D.; Hampel, S.; Leonhardt, A.; Thomas, J.; Mattern, N. & Bücher, B. (2007). Facile one-step-synthesis of carbon wrapped copper nanowires by thermal decomposition of copper(II)-acetylacetonate, *Surf. Coat. Technol.*, 201, 9184–9188, 0257-8972.

Hirahara, K.; Suenaga, K.; Bandow, S. & Iijima, S. (2000). Boron-catalyzed multi-walled carbon nanotube growth with the reduced number of layers by laser ablation, *Chem. Phys. Lett.*, 324, 224–230, 0009–2614, 0009-2614

Hofmann, S.; Sharma, R.; Ducati, C.; Du, G.; Mattevi, C.; Cepek, C.; Cantoro, M.; Pisana, S.; Parvez, A.; Cervantes-Sodi, F.; Ferrari, A.C.; Dunin-Brorkwski, R.; Lizzit, S.; Petaccia, L.; Goldoni, A. & Robertson, J. (2007). In situ observations of catalyst dynamics during surface-bound carbon nanotube nucleation. *Nano Lett.*, 7, 602–608, 1530-6984

Hu, Z.; Liao, X.; Diao, H.; Kong, G.; Zeng, X. & Xu, Y. (2004). Amorphous silicon carbide films prepared by H_2 diluted silane-methane plasma, *J Cryst. Growth*, 264, 7–12, 0022-0248

Iijima, S.; Yudasaka, M.; Yamada, R.; Bandow, S.; Suenaga, K.; Kokai, F. & Takahashi, K. Nano-aggregates of single-walled graphitic carbon nano-horns, *Chem. Phys. Lett.*, 309, 165–170, 0009-2614

Jiao, J. & Seraphin, S. (1998). Carbon encapsulated nanoparticles of Ni, Co, Cu, and Ti, *J Appl. Phys.*, 83, 2442–2448, 0021-8979

Jiao, J.; Seraphin, S.; Wang, X. & Withers, J.C. (1996). Preparation and properties of ferromagnetic carbon-coated Fe, Co, and Ni nanoparticles, *J Appl. Phys.*, 80, 103–108, 0021-8979

Ju, Z., Xu, L.; Pang, Q.; Xing, Z.; Ma, X. & Qian, Y. (2009). The synthesis of nanostructured SiC from waste plastics and silicon powder, *Nanotechnology*, 20, 355604 (6p), 0957-4484

Kawai, T.; Miyamoto, Y.; Sugino, O. & Koga, Y. (2002). Nanotube and nanohorn nucleation from graphitic patches: Tight-binding molecular-dynamics simulations, Phys. Rev. B, 66, 033404-1–033404-4, 1098-0121

Kobayashi, K.; Shimazu, T.; Yamada, Y.; Koshio, A.; Takahashi, Y. & Kokai, F. (2007). Formation of single-wall carbon nanohorn aggregates hybridized with carbon nanocapsules by laser vaporization, *Appl. Phys. A*, 89, 121–126, 0947-8396

Kokai, F.; Ishihara, M.; Koshio, A.; Nakayama, A. & Koga, Y. (2007). Fabrication of some graphitic polyhedra and balloon-like particles, *Diamond Rela. Mater.*, 16, 1264–1268, 0925-9635

Kokai, F.; Koshio, A.; Kasuya, D.; Hirahara, K.; Takahashi, K.; Nakayama, A.; Ishihara, M.; Koga, Y. & Iijima, S. (2004). Three nanostructured graphitic particles and their growth mechanisms from high-temperature carbon vapor confined by Ar gas, *Carbon*, 42, 2515–2520, 0008-6223

Kokai, F.; Koshio, A.; Kobayashi, K. & Deno, H. (2008). Formation of nanocarbon and composite materials by laser vaporization of graphite and eleven metals, *Proceedings of photon processing in microelectronics and photonics VII*, Vol. 6879, pp. 68791F-1–68791F-1-9, 0277-786X, San Jose, SPIE

Kokai, F.; Shimazu, T.; Adachi, K.; Kosho, A. & Takahashi, Y. (2009a). Fabrication of completely filled carbon nanotubes with copper nanowires in a confined space, *Appl. Phys. A*, 97, 55–62, 0947-8396

Kokai, F.; Tachi, N.; Kobayashi, K.; & Koshio, A. (2009b). Structural characterization of single-wall carbon nanohorn aggregates hybridized with carbon nanocapsules and their formation mechanism, *Appl. Surf. Sci.*, 255, 9622–9625, 0169-4332

Kokai, F.; Takahashi K.; Kasuya, D.; Nakayama, A.; Koga, Y.; Yudasaka, M. & Iijima, S. (2003). Laser vaporization synthesis of polyhedral graphite, *Appl. Phys. A*, 77, 69–71, 0947-8396

Kokai, F.; Takahashi, K.; Kasuya, D.; Yudasaka, M. & Iijima, S. (2001). Growth of single-wall carbon nanotubes dependent on laser power density and ambient gas pressure during room-temperature CO_2 laser vaporization, *Appl. Phys. A*, 73, 401–407, 0947-8396

Kokai, F.; Takahashi, K.; Yudasaka, M. & Iijima, S. (1999). Emission imaging spectroscopic and shadowgraphic studies on the growth dynamics of graphitic carbon particles synthesized by CO_2 laser vaporization, *J Phys. Chem.* B, 41, 8686–8693, 1520-6106

Kokai, F.; Uchiyama, K.; Shimazu, T.; & Koshio, A. (2010). Fabrication of two types of one-dimensional Si-C nanostructures by laser ablation, *Appl. Phys. A*, 101, 497–502, 0947-8396

Lin, X.; Wang, X.K.; Dravid, V.P.; Chang, R.P.H. & Ketterson, J.B. (1994). Large scale synthesis of single-shell carbon nanotubes, *Appl. Phys. Lett.* 64, 181–183 , 0003-6951

Li, W.Z.; Wang, D.Z.; Yang, S.X.; Wen, J.G. & Ren, Z.F. (2001). Controlled growth of carbon nanotubes on graphite foil by chemical vapor deposition. *Chem. Phys. Lett.*, 335, 141–149, 0009-2614

Massalski, T.B.; Okamoto, H.; Subramanian, P.R. & Kacprzak, L. (1990). *Binary Alloy Phase Diagrams*, The Materials Information Society ASM International, 0-87170-404-8, Metal Park (USA)

Nerushev, O.A.; Dittmar, S.; Morjan, R.E.; Rohmund, F. & Campbell, E.E.B. (2003). Particle size dependence and model for iron-catalyzed growth of carbon nanotubes by thermal chemical vapor deposition, *J Appl. Phys.*, 93, 4185–4190, 0008-6223

Rümmeli, M.H.; Kramberger, C. Schäffel, F.; Borowiak-Palen, E.; Gemming, T.; Rellinghaus, B, Jost, O.; Löffler, M.; Ayala, P.; Pichler, T. & Kalenczuk, R.J. (2007). Catalyst size dependencies for carbon nanotube synthesis, *Phys. Stat. Sol.*, B, 244, 3911–3915, 0031-8965

Ruoff, R.S.; Lorents, D.C.; Chan, B.; Malhotra, R. & Subramoney, S. (1993). Single crystal metals encapsulated in carbon nanoparticles, *Science*, 259, 346–348, 0036-8075

Ryu,Y.-H.; Park, B.-T.; Song, Y.-H. & Yong, K. (2004). Carbon–coated SiC nanowires: direct synthesis from Si and field emission characteristics, *J Cryst. Growth*, 271, 99–104, 0022-0248

Sabbaghzadeh, J.; Jafarkkani, P.; Dadras, S. & Torkamany, M.J. (2009). Synthesis of multi-wall carbon nanotubes by copper vapor laser. *Appl. Phys. A*, 94, 293–297, 0947-8396

Saito, Y. (1995). Nanoparticles and filled nanocapsules, *Carbon*, 33, 979–988, 0008-6223

Sano, N.; Kikuchi, T.; Wang, H.; Chhowalla, M. & Amaratunga, G.A.J. (2004). Carbon nanohorns hybridized with a metal-included nanocapsule, *Carbon*, 42, 95–99, 0008-6223

Seraphin, S.; Zhou, D. & Jiao, J. (1996). Filling the carbon nanocages, *J Appl. Phys.*, *80*, 2097–2104, 0021-8979

Setlur, A.A.; Lauerhaas, J.M.; Dai, J.Y. & Chang, R.P.H. (1996). A method for synthesizing large quantities of carbon nanotubes and encapsulated copper nanowires, *Appl. Phys. Lett.*, *69*, 345–347, 0003-6951

Subramoney, S.; Ruoff, R.S.; Lorents, D.C. & Malhotra, R. (1993). Radial single-layer nanotubes, *Nature*, 366, 637, 0028-0836

Tao, X.Y.; Zhang, X.B.; Cheng, J.P.; Luo, Z.Q.; Zhou, S.M. & Liu, F. (2006). Thermal CVD synthesis of carbon nanotubes filled with single-crystalline Cu nanoneedles at tips. *Diamond Rela. Mater.*, *15*, 1271–1275, 0925-9635.

Wagner R.S. & Ellis, W.C. (1964). Vapor-liquid-solid mechanism of single crystal growth, *Appl. Phys. Lett.*, 4, 89–90, 0003-6951

Xu, J.; Yang, L.; Rui, Y.; Mei, J.; Zhang, X.; Li, W.; Ma, Z.; Xu, L.; Huang, X. & Chen, K. (2005). Photoluminescence characteristics from amorphous SiC thin films with various structures deposited at low temperature, *Solid State Commun.*, 133, 565–568, 0038-1098

Ye, H.; Titchenal, N.; Gogotsi, Y. & Ko, F. (2005). SiC nanowires synthesized from electrospun nanofiber templates, *Adv. Mater.*, 17, 1531–1535, 0935-9648

Yoshida, H.; Takeda, S.; Uchiyama, T.; Kohno, H. & Homma, Y. (2008). Atomic-scale in-situ observation of carbon nanotube growth from solid sate iron carbide nanoparticles, *Nano Lett.*, 8, 2082–2086, 1530-6984

Yudasaka, M.; Kasuya, Y.; Kokai, F.; Takahashi, K.; Takizawa, M.; Bandow, S. & Iijima, S. (2002). Causes of different catalytic activities of metals in formation of single-wall carbon nanotubes, *Appl. Phys. A*, 74, 377–385, 0947-8396

Yudasaka, M.; Komatsu, T.; Ichihashi, T. & Iijima, S. (1997). Single-wall carbon nanotube formation by laser ablation using double-targets of carbon and metal, *Chem. Phys. Lett.*, 278, 102−106, 0009-2614

Zhang, G.Y. & Wang, E.G. (2003). Cu-filled carbon nanotubes by simultaneous plasma-assisted copper incorporation, *Appl. Phys. Lett.*, 82, 1926–1928, 0003-6951

Zhang, H.-F.; Wang, C.-M. & Wang, L.-S. (2002). Helical crystalline SiC/SiO₂ core–shell nanowires, *Nano Lett.*, 2, 941–944, 1530-6984

Zhang, R.-Q.; Lifshitz, Y. & Lee, S.-T. (2003). Oxide-assisted growth of semiconducting nanowires, *Adv. Mater.*, 15, 635–640, 0935-9648

Advances in Composite Materials for Medicine and Nanotechnology
Edited by Dr. Brahim Attaf

ISBN 978-953-307-235-7
Hard cover, 648 pages
Publisher InTech
Published online 01, April, 2011
Published in print edition April, 2011

Due to their good mechanical characteristics in terms of stiffness and strength coupled with mass-saving advantage and other attractive physico-chemical properties, composite materials are successfully used in medicine and nanotechnology fields. To this end, the chapters composing the book have been divided into the following sections: medicine, dental and pharmaceutical applications; nanocomposites for energy efficiency; characterization and fabrication, all of which provide an invaluable overview of this fascinating subject area. The book presents, in addition, some studies carried out in orthopedic and stomatological applications and others aiming to design and produce new devices using the latest advances in nanotechnology. This wide variety of theoretical, numerical and experimental results can help specialists involved in these disciplines to enhance competitiveness and innovation.

How to reference
In order to correctly reference this scholarly work, feel free to copy and paste the following:

Fumio Kokai (2011). Formation of Various Nanocarbon and Composite Structures by Laser Ablation, Advances in Composite Materials for Medicine and Nanotechnology, Dr. Brahim Attaf (Ed.), ISBN: 978-953-307-235-7, InTech, Available from: http://www.intechopen.com/books/advances-in-composite-materials-for-medicine-and-nanotechnology/formation-of-various-nanocarbon-and-composite-structures-by-laser-ablation

INTECH
open science | open minds